Generation of Highly Accurate DEMs Over Flat Areas by Means of Dual-Frequency and Dual-Baseline Airborne SAR Interferometry

Muriel Pinheiro, Andreas Reigber, *Fellow, IEEE*, Rolf Scheiber, Pau Prats-Iraola, *Senior Member, IEEE*, and Alberto Moreira, *Fellow, IEEE*

***Abstract*— In this paper, a dual-frequency and dual-baseline (DFDB) processing framework for the extraction of high-precision terrain information from airborne interferometric synthetic aperture radar (SAR) data is presented. Specifically, we propose the use of two single-pass data sets acquired simultaneously in two different frequency bands and two large-baseline repeat-pass data sets also acquired simultaneously in two frequency bands. The configuration profits from the stability of the single-pass derived elevation maps in relation to spatially correlated artifacts as well as from the increased sensitivity associated with large-baseline acquisitions. Moreover, the dual-frequency nature of the data set enables the tackling of the phase unwrapping issue, promoting the retrieval of unambiguous measurements. Several algorithms for the interferometric processing of the DFDB airborne data set are proposed, including the outline of multichannel phase calibration and unwrapping error correction strategies and approaches to remove spatially correlated artifacts and extract the common underlying topography. Elevation models generated from a DFDB data set acquired with the airborne F-SAR sensor over tidal flats in northern Germany are presented, and comparisons with an airborne laser scanner reference show errors with a standard deviation of around 14 cm and a mean absolute deviation of less than 10 cm.**

***Index Terms*— Digital elevation model (DEM), dual frequency, repeat-pass interferometry, SAR interferometry (InSAR).**

I. Introduction

ACROSS-TRACK synthetic aperture radar (SAR) interferometry (InSAR) is a well-established tool for topography mapping, and many InSAR systems have been successfully exploited for the retrieval of digital elevation models (DEMs) [1]–[6]. Nevertheless, the generation of InSAR DEMs with a relative vertical accuracy in the order of centimeters in fine spatial grids remains challenging. First, a suitable interferometric configuration has to be selected to ensure the required vertical sensitivity, demanding large baselines between master and slave sensors and/or short wavelengths. In this case, issues related to the interferometric processing have to be properly dealt to mitigate decorrelation and possible biases. In particular, adaptive spectral filtering must be applied [7], and the phase unwrapping/unwrapping errors correction and the phase calibration steps have to be carefully performed. Moreover, when more than one interferograms are available, a method to optimally extract the common topographic information should be considered, ensuring the high quality of the final DEM.

The first challenging step for an accurate DEM reconstruction is the phase unwrapping. In the past two decades, the development of robust algorithms to retrieve unambiguous solutions has been mainly focused on multichannel strategies. The phase of interferometric data sets acquired with different baselines, or using different carriers, have different fringe frequencies. Multichannel strategies aim to remove the ambiguity of the joint problem by using simultaneously all the phase information to retrieve an underlying common height [8]–[12]. Rigorous maximum-likelihood (ML) approaches were introduced in [13]–[16] and opened the door to several more robust algorithms using contextual information in maximum *a posteriori* (MAP) frameworks [17]–[22]. No universal solution can be singled out, and the efficiency of the approaches is closely related to the characteristics of the available data set [e.g., a number of images and distribution of the available heights of ambiguity (HoAs)] and imaged scene (e.g., topography and land coverage). In general, however, the performance of ML and MAP approaches degrades when only a limited number of acquisitions are available.

Despite the use of robust phase unwrapping algorithms, unwrapping errors might occur, e.g., due to the insulation of regions by water bodies or other decorrelating features. In fact, the general difficulty of the phase unwrapping problem promoted the development of a few strategies for unwrapping error treatment. For example, [23] proposed a strategy to detect and correct remaining 2π ambiguities in a baseline calibration step. The approach was later extended in [24], where morphological filters to improve the detection were included. More recently, Lachaise *et al.* [25] developed the correction strategy of the TanDEM-X operational processor profiting from the mission dual-baseline global coverage to detect and correct unwrapping inconsistencies.

A second important aspect of the generation of DEMs from InSAR data concerns the calibration of the interferometric phase. The term *phase calibration* may incorporate the correction of phase offsets, baseline errors, and other artifacts. The main challenges are to achieve a precise calibration using minimum or no external information and to obtain results

Manuscript received October 24, 2017; revised January 31, 2018; accepted March 14, 2018. *(Corresponding author: Muriel Pinheiro.)*

The authors are with the Microwaves and Radar Institute, German Aerospace Center, 82230 Wessling, Germany (e-mail: muriel.pinheiro@dlr.de).

Color versions of one or more of the figures in this paper are available online at http://ieeexplore.ieee.org.

Digital Object Identifier 10.1109/TGRS.2018.2817122

that are robust to unwrapping errors. The calibration of phase offsets without the use of ground control points (GCPs) has been investigated in the context of multichannel configurations in [26], where an entropy maximization scheme was proposed. In the realm of offset estimation in single-pass interferograms, [27] proposed an approach using data sets acquired with opposite geometries, while [28] investigated a two-step methodology based on the use of low-resolution external and possibly biased DEMs. The approach was later simplified in [29], where a single-step scheme was suggested profiting from the approximately linear relation between height and phase. In a similar way, [30] proposed a method to calibrate airborne repeat-pass data using TanDEM-X intermediate DEMs.

The more general problem of how to combine all the available information to obtain a high-quality elevation model should also be addressed. The issue is closely related to the characteristics of the available data sets and, ultimately, the product requirements. As previously mentioned, many strategies couple the extraction of the underlying topography to the phase unwrapping in a multichannel framework. In addition to the already cited literature, [16] investigated an ML approach to combine single-pass multibaseline/multiaspect data sets to obtain the elevation models of urban areas using the MEMPHIS Ka-band sensor. Moreover, [5] and [31] studied several aspects of the SAR and InSAR processing chains for MEMPHIS Ka-band data, including the efficiency of ML height estimators.

Current spaceborne interferometric SAR systems can provide wide coverage topographic measurements with spatial resolution and vertical accuracy in the order of a few meters. For example, the TanDEM-X mission is allowed for the creation of a global DEM with a point-to-point relative vertical accuracy of 2 m for flat-to-moderate terrain and 4 m for steep terrain within a 90% confidence interval and a spatial resolution of around 12 m [32]. Experimental processing strategies can also be used to improve the elevation models derived from the TanDEM-X data. For example, [33] proposed an iterative coarse-to-fine multilooking approach, and DEMs in a 4-m sampling spatial grid and a height accuracy of less than 2 m were reported. Moreover, the possibility of having large-baseline single-pass interferograms during the mission science phase is allowed for elevation maps with even higher accuracy [34]. For example, Lee and Ryu [35] generated DEMs using large-baseline TanDEM-X data over tidal flats with 5–7-m sampling and reported the rms errors of around 20 cm in comparison with GPS measurements. In [36], highly accurate DEMs with 6-m sampling and height accuracy (standard deviation) around 17 cm in comparison with airborne laser measurements were achieved for areas of flat-to-moderate terrain. Nevertheless, the level of topography details obtained with airborne laser scanner (ALS) still surpasses the one found in spaceborne SAR products due to the finer spatial grids and submeter vertical accuracy of usual ALS systems [37]–[40].

Despite being able to generate very precise results, current ALSs have a much smaller coverage when compared with usual airborne SAR systems, which turn the ALS imaging of large areas comparatively more expensive. Additionally, ALS sensors are considerably more sensitive to weather conditions. Therefore, airborne InSAR for DEM generation offers a good compromise between acquisition cost and achievable accuracy. In fact, several airborne SAR systems have been used recently to retrieve accurate topographic information. For example, the aforementioned works [5], [31] reported a relative vertical accuracy varying from 19 to 59 cm (one standard deviation), depending on the characteristics of the acquisition, and an effective coverage area of around 2.1 km $\times$ 0.6 km (azimuth $\times$ range) using data from the Memphis Ka-band system. De Macedo *et al.* [41] demonstrated the importance of using topography-and-aperture-dependent Motion Compensation (MoCo) to retrieve accurate height measurements over challenging terrain using the single-pass/three-baseline configuration of the OrbiSAR sensor. They reported DEMs with 5-m spatial resolution and a relative vertical accuracy of around 40 cm when comparing data from orthogonal views. Marotti *et al.* [42] showed the results obtained with the X- and Ku-band MetaSensing airborne sensors covering an area of around 3.5 km $\times$ 0.5 km (azimuth $\times$ range). The comparison with a laser reference showed a relative height accuracy of the order of 30 cm in both cases for flat terrain. Perna *et al.* [6] presented first the results of the TELAER multibaseline interferometric system, able to acquire X-band data with range resolution around 0.5-m and 1.5-km swath. Like the OrbiSAR, the TELAER single-pass interferometer profits from a three-baseline configuration to deal with the phase ambiguity problem. They also emphasized the necessity of a precise MoCo, and preliminary comparisons with ALS measurements have shown height errors (one standard deviation) in the order of 1.5 m.

The work presented in this paper aims to generate highly accurate elevation models from airborne InSAR data collected with as few acquisition flights as possible. Specifically, we seek to construct DEMs from data collected with the F-SAR sensor [43], in a grid with 1 m $\times$ 1 m spatial sampling and relative and absolute vertical accuracies in the order of decimeters, i.e., comparable with ALS technology. Note that, although the above-mentioned Ka-band airborne interferometers can yield DEMs with a submeter vertical accuracy, the swath limitation makes such systems less suitable for the mapping of large areas. Moreover, DEMs obtained with data from general X-band single-pass interferometers using standard processing techniques do not satisfy simultaneously our vertical and spatial accuracy requirements. In order to obtain the desired DEM quality, we suggest the use of F-SAR data acquired over two passes, one of them also using the single-pass interferometer. In this way, at least one single-pass and one repeat-pass interferogram are available. For the latter, a suitable large baseline is chosen. Moreover, during each flight, data are acquired using simultaneously the X-band and S-band systems, benefiting from the multifrequency capabilities of the F-SAR sensor. Consequently, data from a dual-frequency (X- and S-band) and dual-baseline (single- and repeat-pass) configuration can be used.

Due to the reduced number of available images, the large ratio between repeat- and single-pass baselines, and the presence of low-frequency artifacts in the repeat-pass interferograms, the direct extraction of topography from the wrapped

phases using the ML/MAP approaches as in [8]–[22] is not possible. The large ratio between the baselines and between the S- and X-band wavelengths also prevents the use of [44] for the identification of unwrapping errors. Moreover, general unwrapping error correction strategies fail to treat interferograms with an HoA in the order of meters and containing residual biases, as is the case considered here. The state-of-the-art approaches for the calibration of airborne InSAR data, e.g., the ones proposed in [28] and [29], are not well suited for repeat-pass interferometry, since they neglect unwrapping errors, baseline miscalibration, and other low-frequency disturbances. Additionally, F-SAR single-pass interferograms are affected by range-dependent multipath errors, which further challenge the calibration process [45]. Current solutions either rely on calibration data or are not able to ensure the submeter vertical accuracy required here [46], [47]. In order to solve the aforementioned problems of unwrapping, calibration, and topography retrieval in an efficient manner, we propose a DEM generation chain suitable for the suggested dual-frequency and dual-baseline (DFDB) configuration.

This paper is organized as follows. Section II briefly discusses the choice of the DFDB configuration, while Section III presents the overall structure of the DEM generation chain. Novel approaches of the chain are discussed in Sections IV–IX. Specifically, Section IV briefly addresses the dual-frequency phase unwrapping issue, Section V details the strategy to mitigate multipath artifacts in the single-pass InSAR data, Section VI discusses the calibration of baseline errors and phase offsets, Section VII presents an unwrapping error verification strategy for the repeat-pass data, Section VIII proposes a method to mitigate residual biases contained in the repeat-pass interferograms, and Section IX describes the retrieval of the underlying topography considering the different available data sets. In Section X, DEMs derived from DFDB F-SAR data acquired over the tidal flats in the Jade Bight (northern Germany) are shown and compared with an ALS reference model for validation. Finally, Section XI gives the conclusions.

II. Proposed Configuration

The proposed DFDB configuration enables the extraction of precise terrain information from airborne interferometric data and was conceived considering the particularities of the F-SAR system [43], [48]. The F-SAR uses the IGI's CCNS4 navigation system and postprocessing software. The sensor is capable of acquiring fully polarimetric data in five different frequency bands: X, C, S, L, and P. Furthermore, data can be simultaneously collected in up to four different wavelengths, and the S- and X-band modules include single-pass across-track interferometers with an effective baseline of around 1.6 m. A detailed description of the F-SAR system is given in [43].

A. "Dual-Baseline" Nature of the Configuration

The relative height accuracy achievable through InSAR can be expressed in terms of the interferometric vertical wavenumber k_z and the standard deviation of the phase noise σ_ϕ as

$$\sigma_h \approx \frac{1}{k_z}\sigma_\phi \approx \frac{\lambda R \sin\theta}{4\pi B_\perp}\sigma_\phi \tag{1}$$

where λ is the wavelength, R is the range distance, θ is the incidence angle, and $B_\perp$ is the projection of the baseline between master and slave antennas in the direction perpendicular to the line of sight [49], [50]. For surface scattering, the increase in $B_\perp$—or conversely the decrease in the HoA ($\triangleq 2\pi/k_z$)—usually leads to an improvement of the retrieved height measurements, as long as the decrease in the interferometric coherence (e.g., due to geometric decorrelation) is limited or can be treated [7].

Due to the short baseline of the F-SAR single-pass interferometer (around 1.6 m), at least one large-baseline repeat-pass data set must be employed in order to ensure high vertical sensitivity. The baseline length can be chosen according to the height accuracy requirements considering system characteristics—e.g., wavelength, system resolution, noise equivalent sigma nought, and flight altitude—and the statistics of the interferometric phase [49]. Under ideal conditions and neglecting geometric distortions, a single interferometric data set acquired with a sufficiently large baseline would enable the generation of highly accurate topographic maps. However, large-baseline repeat-pass interferograms are often affected by low-frequency artifacts due to, e.g., uncompensated (residual) motion errors or atmospheric effects [51], [52]. If left untreated, such disturbances introduce biases in the derived elevation models. On the other hand, monostatic single-pass interferometers are generally robust in relation to biases, since master and slave are equally affected by these errors. However, the fixed baseline is usually not sufficiently large to ensure the desired vertical accuracy. By combining both measurements, one could then account for possible biases using the single-pass interferometric information while profiting from the lower sensitivity to the noise of elevation models generated from large-baseline interferograms.

Notice that the improvement in height accuracy is caused by enlarging the baseline ceases when volume or baseline decorrelation becomes predominant. For airborne systems with high range resolution, baseline decorrelation is not a limiting factor for obtaining height accuracies in the order of decimeters. On the other hand, volumetric decorrelation might dominate when acquiring with large baselines. Thus, the usage of large-baseline interferograms to recover information over high vegetation, even when acquiring at higher frequency bands, becomes prohibitive [4], [36]. Hence, the additional use of a small-baseline data set (e.g., the F-SAR single-pass) is helpful if the height retrieval of such scatters is required and a decreased vertical accuracy is acceptable.

B. "Dual-Frequency" Nature of the Configuration

Although the single-pass/repeat-pass configuration is theoretically suitable for the recovery of highly accurate elevation models (up to the statistical limit imposed by the chosen baseline), practical issues related to the interferometric processing can impair the results. The interferometric phase unwrapping

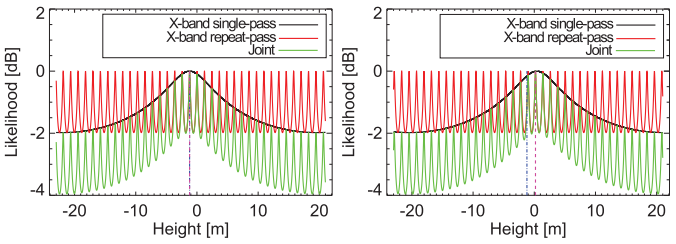

Fig. 1. (Left) Interferometric phase pdf parameterized by the height. (Right) Interferometric phase likelihoods obtained from the F-SAR data. The coherence coefficients of single- and repeat-pass interferograms are 0.95 and 0.6, and the nominal height is −1.2 m as indicated by the blue vertical line.

step is specially critical, since large-baseline configurations result in phases with very high fringe frequency. As previously mentioned, multichannel approaches can be used to reduce the ambiguity of the interferometric phase joint *pdf*. However, that is not the case of the single-/repeat-pass configuration considered here due to the large difference between the individual HoA and the reduced number of available interferograms.

As an example, Fig. 1 (left) shows the simulated X-band single- and repeat-pass interferometric phase likelihoods parameterized by the height. Effective baselines of around 1.6 and 28 m were considered. In this ideal example, no phase error is considered, i.e., the observed phases match theirs nominal values. The joint likelihood appears in green, and consists of the multiplication of the individual likelihoods, i.e., the statistical independence of the data sets is assumed. The investigated height interval is constrained to 42 m, corresponding to only one cycle of the single-pass likelihood, but several cycles of the repeat-pass one. In this case, the global maximum of the joint likelihood is located at the nominal residual height position in this simulation at −1.2 m. Due to the baseline ratio, small errors in the measured single-pass phases (e.g., due to decorrelation or biases) shift the position of the global maximum of the joint likelihood by an amount of the order of magnitude of the repeat-pass HoA. This is observed in Fig. 1 (right), where the likelihoods obtained from the experimental F-SAR X-band data are depicted. The single-pass coherence coefficient is 0.95, while the repeat-pass one is 0.6. The single-pass phase measurement deviates by 15° from its nominal value, causing a shift of approximately 1.4 m in the position of the global maximum (indicated by the pink vertical line) in relation to the true height position (indicated by the blue vertical line).

The introduction of data collected with additional baselines can further reduce the ambiguities at the cost of an increased number of flights. However, the phase of an interferometric data set acquired from independent passes will contain uncorrelated low-frequency artifacts, posing a problem to multibaseline approaches in airborne interferometry. In order to circumvent the issue, keeping the number of acquisition flights to a minimum of two, a DFDB configuration is suggested profiting from the multifrequency capabilities of the F-SAR airborne system. As discussed in [13] and [17], the choice of multifrequency data sets over multibaseline ones has the additional advantage that the hypothesis of independence

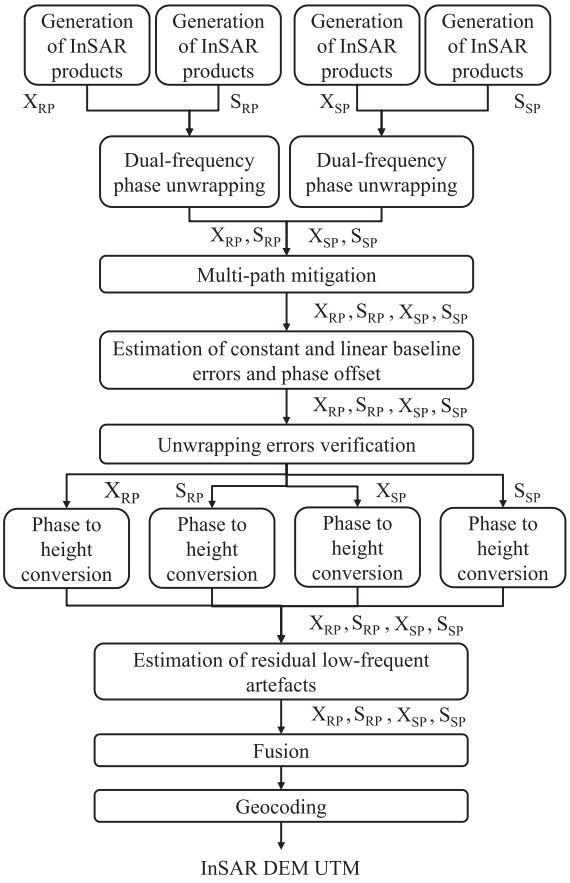

Fig. 2. Block diagram of the DFDB DEM processing chain. The tags S_{SP}, $X)_{SP}$, S_{RP}, and X_{RP} stand for S-band single-pass, X-band single-pass, S-band repeat-pass, and X-band repeat-pass, respectively.

between the interferograms is met, and the computation of the multichannel joint statistics is straightforward. Although large spectral separation favors a less ambiguous joint likelihood, too large spectral separation may lead to different interferometric phase contents in case of semitransparent media. Thus, a compromise has to be made according to the desired application.

III. Interferometric Processing Chain

The necessary processing steps for the DFDB DEM generation from the four available interferometric data sets are shown in Fig. 2. In the diagram and in the remaining of this paper, the tags S_{SP}, X_{SP}, S_{RP}, and X_{RP} stand for S-band single-pass, X-band single-pass, S-band repeat-pass, and X-band repeat-pass, respectively, and are used to identify inputs/outputs throughout the chain. A short summary of each module is given in the following.

1) *Generation of Interferometric Products:* The first module consists in the generation of the required interferometric products and takes place after all the individual complex images have been formed. Precise knowledge of the lever-arm information is assumed (better than 1mm), as obtained from *a priori* evaluation of calibration data takes with corner reflectors deployed across the full range of incidence angles [53]. In addition,

the strong nonlinear phase pattern, especially in X-band (see Fig. 5), suggests that the antenna phase center varies with an elevation angle. This is corrected during antenna pattern compensation as part of the SAR image formation [43]. Although the interferometric process runs individually for each data set at this stage, all single look complex (SLC) complex images should be coregistered to the same geometry. While single-pass interferograms are created without any filtering, a range-adaptive spectral filter is employed to account for geometric decorrelation in the repeat-pass interferograms [7]. The module also contains the flat-earth removal based on either a reference DEM with low-accuracy or a mean terrain value. Finally, the multisquint approach is employed to compensate for residual motion errors in the repeat-pass interferograms (up to constant and linear components) [54]. Since the acquisition of X- and S-band is simultaneous, the residual motion errors are expected to be the same for both data sets. Consequently, it is sufficient to perform the estimation using the data from a single frequency of acquisition, applying the estimated baseline corrections to both data sets. Moreover, applying the same correction in both data sets ensures that possible uncompensated errors in the phases correlate, which impacts the choice of unwrapping strategy. Once the interferograms have been formed, the interferometric phase and coherence are extracted and are used as an input for the next steps.

2) *Dual-Frequency Phase Unwrapping:* The second module encompasses the unwrapping of the interferometric phases and is performed using a dual-frequency approach based on the region-growing algorithm (see Section IV).
3) *Multipath Mitigation:* Once the phases are unwrapped, the first calibration step takes place, namely, a multipath mitigation strategy is applied to correct artifacts in the single-pass phases [45], [46]. The repeat-pass phases are involved in the process, serving as multipath-free references (see Section V).
4) *Estimation of Constant and Linear Baseline Errors and Phase Offset:* In the next calibration step, possible offsets and trends due to constant and linear baseline errors are compensated (see Section VI).
5) *Unwrapping Errors Verification:* In this module, possible unwrapping errors are detected and corrected using an active contour's scheme. This step aims at the treatment of large-scale unwrapping errors mainly associated with discontinuities in the image (see Section VII).
6) *Phase-to-Height Conversion:* In the following, the phases are individually transformed to height maps, still in slant-range geometry.
7) *Estimation of Residual Low-Frequency Artifacts:* The final calibration modules estimate and correct residual low-frequency artifacts in the repeat-pass data sets due to, e.g., residual motion errors or atmosphere heterogeneity (see Section VIII).
8) *Fusion:* In this step, the information of the data from the different baselines and frequencies of acquisition is merged into the final elevation model, considering a noise mitigation strategy (see Section IX).
9) *Geocoding:* The obtained elevation model is transformed into universal transverse mercator coordinates.

In Sections IV to IX, the details of the different calibration steps, phase unwrapping, and extraction of the underlying topography are presented.

IV. Phase Unwrapping

The unwrapping of the X- and S-band interferograms is performed jointly profiting from the reduced ambiguity of the dual-frequency unwrapping problem. However, as indicated by the block diagram in Fig. 2, single- and repeat-pass phases are handled independently in order to avoid salt-and-pepper-like errors associated with the large ratio between the HoAs of both data sets.

The phase unwrapping is carried out using the dual-channel region-growing approach described in detail in [36] for a dual-baseline spaceborne configuration, and it is an adaptation of the single-channel region growing algorithm proposed in [55]. The approach can be directly employed for the dual-frequency scenario as long as uncorrelated biases in both data sets are negligible in comparison with the smallest HoA. The configuration proposed in this paper, i.e., the simultaneous acquisition of the multifrequency data sets, promotes robustness in relation to phase artifacts caused by residual motion errors and troposphere heterogeneity, thus enabling the use of such an algorithm with airborne data.

The dual-channel region-growing algorithm is congruent, i.e., it removes 2π multiples from each pixel. The approach relies on the estimation of this ambiguity band using three different strategies: 1) independently evaluating the already unwrapped neighbors in both data sets; 2) assuming that the height information of the center pixel is the same in both data sets; and 3) assuming that the slope computed from the already unwrapped pixels is the same in both data sets. The final ambiguity band is then estimated considering a weighted average according to the expected statistics of the three predictions. Moreover, the discrepancy between these predictions is used together with the interferometric coherences as an extra reliability measure to guide the region growing path.

Unlike in the dual-baseline case considered in [36], in the dual-frequency scenario, differences of phase content caused by the changes in penetration depth can occur within semi-transparent media. If the differences are in the order of the smallest HoA, the dual-channel approach is likely to introduce errors in the corresponding unwrapped phase. Since here we consider repeat-pass HoAs in the order of meters, the estimated height of, e.g., crops and forest, will be biased toward the one corresponding to the phase center of the S-band data set. On the other hand, the HoAs of the single-pass data sets (tens of meters) are much larger than the expected penetration depth differences (centimeters to a few meters). An alternative would be then to first unwrap the single-pass phases and use the filtered differences between the S- and X-band unwrapped data sets (after conversion to height) in order to weight down the predictions of the repeat-pass unwrapped number which assume same height content, whenever a problematic region

is encountered. An example of the height discrepancies caused by the differences in X- and S-band penetration depths is shown later in Section X.

V. Mitigation of Multipath Artifacts

The reception of secondary returns superimposed to the direct signal of interest is a problem for many communication, navigation, and imaging systems. For example, in airborne SAR systems, the antennas are often surrounded by metallic structures from the antenna mount or aircraft fuselage. As a consequence, the sensors often receive strong signals from reflections on the surrounding surfaces rather than on the remote imaged scene [45]–[47], [56]–[60]. The additional undesired reflections are generally called multipath signals and are usually not accounted for during the image focusing. Consequently, amplitude and phase disturbances arise in the form of oscillations dependent on the incidence angle.

The phase distortions caused by the multipath must be corrected to ensure the quality of the derived elevation models. In fact, the matter is addressed within the calibration steps of many airborne InSAR systems. Chapin *et al.* [60], for example, used an external high-precision DEM in order to estimate a range-dependent phase correction, which is then approximated by Chebyshev polynomials to account for all required incidence angles. In a similar way, [57] and [58] compute the phase screen from acquisitions over sea surfaces, for which an accurate height reference is available. Kobayashi *et al.* [59] suggested a parametric estimation using a single-reflection multipath model followed by the corresponding phase correction. However, the results were reported as unsatisfactory by the authors. In [47], a cross-calibration scheme is considered exploiting overlapping data acquired from crossing tracks. Mao *et al.* [46] presented a more sophisticated model comprising multiple reflections, and made use of targets with the well-known elevation in order to estimate the model parameters. Magnard *et al.* [31] used the interferometric data from perpendicular tracks to build an incident-angle-dependent phase correction for a Ka-band MEMPHIS data set for which no antenna pattern phase information was available.

A. F-SAR Multipath Characterization

In the case of the F-SAR system, the antennas constituting the X- and S-band interferometers are located in the antenna mount attached to the right lateral of the aircraft, as illustrated in Fig. 3.

Given the mount design and antenna configuration, backscattered signals are reflected on the area indicated in green in Fig. 3, and are received by the upper antennas (S2 and X2) overlapped with the direct signal. Reciprocally, the transmitted signal is composed by a direct component plus the reflected one. The latter is delayed and attenuated in relation to the former. Considering that the only multipath components originate from reflections within the indicated area, the lower antennas (S1 and X1) are not affected.

Cross sections of the two-way antenna pattern gains along the elevation measured by the German Aerospace Center compact test range (CTR) facility [61] are shown in Fig. 4. X- and S-band VV measurements appear on the left and right of Fig. 4, respectively. The corresponding antenna pattern phases can be seen in Fig. 5. In all plots, the case when the lower antennas (X1 and S1) act as both receiver and transmitter is shown in black curve, the case when the lower antennas act as transmitter and the upper ones as receiver is shown in red curve, and finally, the case when the upper antennas act as both transmitter and receiver is shown in blue curve. Oscillations caused by the multipath reflections can be noticed in both phase and amplitude of the upper X-band patterns and in the phase of the upper S-band pattern. As expected, no relevant effect is recognized in the measurements of the lower antennas.

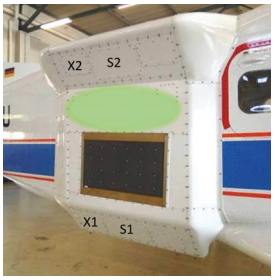

Fig. 3. F-SAR antenna mount attached to the Do228 aircraft. The location of the X- and S-band antennas is indicated. The flat area indicated in green enables that multipath reflections reach the X2 and S2 antennas.

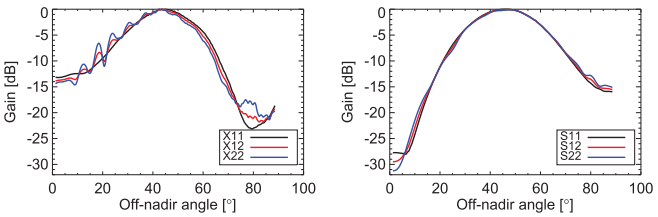

Fig. 4. Two-way antenna gain along elevation for (Left) X-band and (Right) S-band. In both plots, the patterns considering the lower antennas (X1 and S1) as both receiver and transmitter are shown in black curve, the patterns considering the lower antennas as transmitter and the upper as receiver are shown in red curve, and finally, the patterns considering the upper antennas as transmitter and receiver are shown in blue curve. Especially, for the X-band case, it is possible to see the oscillations caused by the multipath presence in the upper antennas.

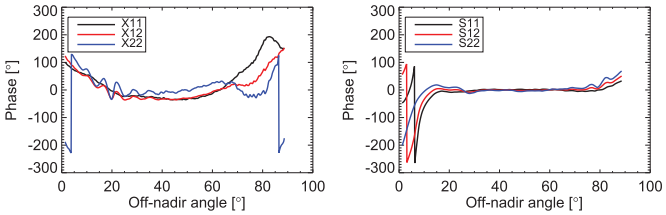

Fig. 5. Antenna pattern phase along the elevation for (Left) X-band and (Right) S-band. In both plots, the patterns considering the lower antennas (X1 and S1) as both receiver and transmitter are shown in black curve, the patterns considering the lower antennas as transmitter and the upper as receiver are shown in red curve, and finally, the patterns considering the upper antennas as transmitter and receiver are shown in blue curve.

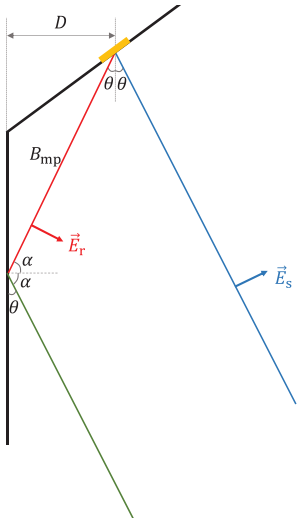

Fig. 6. Geometry of multipath reflections. The slave antenna is indicated in yellow. The direct field received by the antenna ($\vec{E}_s$) appears in blue line, while the reflected field ($\vec{E}_r$) appears in red line. D is the horizontal distance between the antenna phase center and the antenna mount.

B. Multipath Model

Fig. 6 shows the geometry of the problem considering a direct backscattered signal and a single multipath component being received by the SAR sensor. In Fig. 6, a wave polarization parallel to the plane of incidence is considered [62]. The sketch shows three rays: the direct one in blue line, the incident one in green line, and the multipath (or reflected) one in red line. Furthermore, the antenna phase center appears in yellow. The distance between this phase center and the locus of reflection is indicated as B_{mp}, and is analogous to the baseline of an across-track interferometer.

The total field received by the upper antenna is given by the sum of the direct component and the projection of the reflected component in $\hat{\boldsymbol{\theta}}_{\boldsymbol{i}}$, whose amplitude is attenuated by the reflection coefficient. Furthermore, the two received signals are shifted in phase due to the reflection coefficient, and, additionally, the geometrical difference between the direct path and the path traveled by the reflected ray [59], [63]. Analytically,

$$\vec{E}_{\text{mp}}(\theta) = \vec{E}_{\text{s}}(\theta) + \vec{E}_{\text{s}}(\theta)\bar{\rho}(\theta)\cos(2\theta)e^{-j\frac{2\pi}{\lambda}\Delta R_{\text{mp}}} \qquad (2)$$

where $\vec{E}_s$ is the multipath-free field, $\bar{\rho}$ is the equivalent complex reflection coefficient [64], [65], λ is the wavelength, and ΔR_{mp} is the path difference between direct and multipath components. Note that the reflection coefficient depends on the polarization of the wave and, except for the case of perfectly conducting surfaces, on the incidence angle. Therefore, the equivalent antenna pattern, i.e., the one including the multipath reflections depends on the employed polarization.

Considering the geometry depicted in Fig. 6, the total path difference ΔR_{mp} between the direct and multipath components can be written as

$$\Delta R_{\text{mp}} \approx -B_{\text{mp}}(-\cos(2\theta) + 1) = -2D\sin\theta \qquad (3)$$

where D is the horizontal separation between the antenna phase center and the antenna mount.

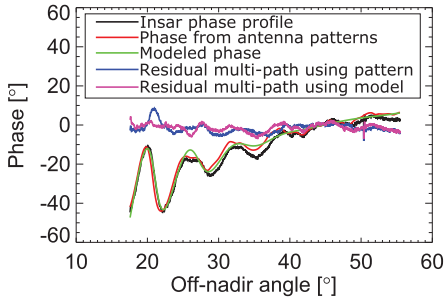

Fig. 7. Black curve: interferometric phase profile estimated from the data. Red curve: phase profile obtained from master and slave antenna patterns. Green curve: phase profile obtained from model. Blue curve: residual multipath profile after removing the phase of antenna pattern. Magenta curve: residual multipath profile after removing modeled phase in magenta.

C. Multipath Mitigation Using Modeled and Measured Phase Profiles

Assuming that the distance from the fuselage (D) and the reflection coefficient is known or can be estimated from the data, the relation between the antenna pattern containing multipath and the ideal one can be found using (2) and (3). Moreover, the phase of the equivalent pattern can then be extracted and used to estimate a correction for the interferometric data when no precise antenna measurement is available.

In the case of the F-SAR system, $D \approx 16$ cm and the path difference between the direct and reflected signals is up to 20 cm in far range, which corresponds to less than half of an X-band resolution cell. Therefore, the multipath effect does not introduce ambiguous echoes, and a phase correction should be able to remove the artifacts observed in the interferograms.

Although measurements of the antenna pattern phase are available for the F-SAR data, the obtained correction is limited due to, e.g., errors in the CTR measurements and lack of precise knowledge of attitude and incidence angles. Fig. 7 shows, in black curve, an example of residual phase extracted from the F-SAR single-pass InSAR data. The profile corresponds to the difference between the interferometric phase and the synthetic phase generated using a highly accurate ALS DEM, and, hence, should contain no strong topographic information. The interpolated antenna pattern phase obtained using the information of master and slave antennas is shown in red curve, while the residual multipath profile after removing the phase of the antenna pattern appears in blue curve.

Fig. 7 also contains the phase profile obtained from the reflection model in green curve. In this case, the unknown complex reflection coefficient, vertical and horizontal offsets from the nominal phase center, and depression angle error were estimated directly from the interferometric data [45]. The residual multipath profile after removing the phase given by the proposed model appears in magenta.

The improvement obtained when using any of the phase profiles to correct the interferometric phase is clear. Nevertheless, artifacts up to 10° can still be found when using the measured

antenna pattern, leading to height errors up to 1 m and not satisfying the absolute accuracy requirements considered in this paper. Fitting the data to the reflection model to estimate the correction allows to reduce the maximum error to 6°. However, the approach requires knowledge of the topography for at least part of the imaged scene.

D. Data-Based Multipath Mitigation for the DFDB Configuration

An alternative mitigation strategy proposed here is based on an iterative estimation of the multipath phase profile from the available DFDB data set. Specifically, the difference between the phase content of single- and repeat-pass interferograms is exploited, allowing for the estimation of the multipath component directly from the data without knowledge of the topography.

After the phase flattening, the residual single-pass interferometric phases can be approximated as [66]

$$\phi_{\text{res}}^{\{\text{X,S}\}_{\text{SP}}}(\theta) \approx k_{z,\text{real}}^{\{\text{X,S}\}_{\text{SP}}} \Delta h\ (\theta) + \phi_{\text{mp}}^{\{\text{X,S}\}_{\text{SP}}}(\theta) \tag{4}$$

where $k_{z,\text{real}}^{*}$ are the vertical wavenumbers calculated from the real tracks, Δh is the difference between the employed reference height and the true height of the terrain, and $\phi_{\text{mp}}^{\text{S}_{\text{SP}},x_{\text{SP}}}$ are the multipath phase profiles. For convenience, the unknown single-pass phase offsets were included in the multipath profile. The formulation considers that no global coregistration errors remain, which is usually the case for single-pass interferometry. Note that θ depends on the unknown topography and aircraft attitude and, hence, it is function of both range and azimuth. Rapid topography changes might introduce higher frequency components in the multipath profile.

The repeat-pass interferometric phases can be approximated as

$$\begin{aligned}\phi_{\text{res}}^{\{\text{X,S}\}_{\text{RP}}} \approx\ & \nu_{\text{X,S}} + k_{z,\text{real}}^{\{\text{X,S}\}_{\text{RP}}} \Delta h \\ & + \frac{4\pi}{\lambda_{\text{X,S}}} \left(\varepsilon_{y_1}^{\{\text{X,S}\}_{\text{RP}}} + \varepsilon_{y_2}^{\{\text{X,S}\}_{\text{RP}}} x\right) \sin\theta \\ & + \frac{4\pi}{\lambda_{\text{X,S}}} \left(\varepsilon_{z_1}^{\{\text{X,S}\}_{\text{RP}}} + \varepsilon_{z_2}^{\{\text{X,S}\}_{\text{RP}}} x\right) \cos\theta \end{aligned} \tag{5}$$

where $\varepsilon_{y_1}^{*}$ and $\varepsilon_{z_1}^{*}$ are constant baseline errors in the horizontal and vertical directions, $\varepsilon_{y_2}^{*}$ and $\varepsilon_{z_2}^{*}$ describe the linear components of the baseline errors, and ν_{X} and ν_{S} are phase offsets [54]. Note that a generic case is being considered here, where X- and S-band baseline errors might be independent (a simplification for simultaneous acquisitions is considered later in Section VI-B). In practice, the repeat-pass phase might contain additional spatially correlated errors of higher order along azimuth due to, e.g., limitations of the multisquint algorithm [54]. However, considering that such residual errors are slowly varying, the approximation in (5) is expected to hold within small intervals over azimuth. In fact, since the goal is the estimation of a 1-D profile along the elevation, it is enough to select a small block of data covering the whole swath. Using the vertical wavenumbers to account for the different geometries, the difference between the single- and repeat-pass phases can be calculated in order to cancel Δh. In this case, the only dependence with the residual topography is due to the incidence angle.

The multipath components are highly sensitive to the variations of the aircraft attitude and, hence, the corresponding phase profiles can vary from range line to range line. Whenever possible, it is advisable to select data corresponding to smooth topography for the estimation, in which case the multipath profiles are also smoother and similar for the whole block. Nevertheless, even for a perfectly flat terrain, changes in the roll angle introduce an azimuth dependence of the multipath phase. Accordingly, in order to make the range lines of the phase difference comparable, the phase differences are interpolated to a common incidence angle profile θ_c. This profile is selected by simply averaging the expected θ over the azimuth dimension. Since the expected multipath artifacts are low frequent, the sampling of θ_c can be larger than that of θ at least in the first iteration. After the interpolation, the only expected azimuth variation in $\phi_{\text{diff}}^{\text{X,S}}(\theta_c)$ is due to the linear baseline error component.

The use of an azimuth block rather than a single range-line is justified by two simple reasons. First, the effect of phase noise is mitigated by averaging over azimuth. Second, the practical implementation of the algorithm tags certain regions as improper for the estimation. A pixel is deemed invalid if: 1) it was considered unreliable by the phase unwrapping algorithm; 2) its coherence on either repeat-pass or single-pass interferograms is below a predefined threshold; or 3) it is considered an outlier according to the modified Z-score test applied to each azimuth line of the consider block [67]. As a consequence, a given range line might contain valid information only for a certain range of incidence angles. In general, blocks corresponding to higher coherence and less prone to contain unwrapping errors should be preferred, and ideally, at least one measurement over the discrete range of incidence angles is available. Otherwise, an interpolation has to be performed accounting for the missing data, and the overall quality of the correction might degrade.

Assuming that the variations along the azimuth of $k_{z,\text{real}}^{\text{S}_{\text{SP}},x_{\text{SP}}}$ can be neglected, which should hold for a small block in azimuth, the average of the phase difference over the azimuth interval can be written as

$$\begin{aligned}&\phi_{\text{diff}}^{\text{X,S}}(\theta_c) \\ &\approx \phi_{\text{mp}}^{\{\text{X,S}\}_{\text{SP}}}(\theta_c) - \frac{k_{z,\text{real}}^{\{\text{X,S}\}_{\text{SP}}}}{k_{z,\text{real}}^{\{\text{X,S}\}_{\text{RP}}}}(\theta_c) \\ &\quad \cdot \left[\frac{4\pi}{\lambda_{\text{X,S}}} \varepsilon_{y}^{\{\text{X,S}\}_{\text{RP}}} \sin\theta_c + \frac{4\pi}{\lambda_{\text{X,S}}} \varepsilon_{z}^{\{\text{X,S}\}_{\text{RP}}} \cos\theta_c + \nu_{\text{X,S}}\right] \end{aligned} \tag{6}$$

where ε_{y}^{*} and ε_{z}^{*} are equivalent constant errors over the block. The signal in (6) is 1-D and contains both the multipath profile and the phase due to constant baseline errors. In principle, the interpolated phase difference could be filtered and used as an equivalent multipath profile in order to correct X- and S-band single-pass residual phases, leaving the baseline calibration to a posterior step. In this case, the phase error model used for the single-pass calibration, which often considers only

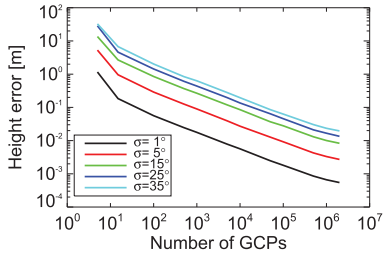

Fig. 8. Maximum height error resulting from miscalibration of the baseline error as a function of the number of reference points used for calibration.

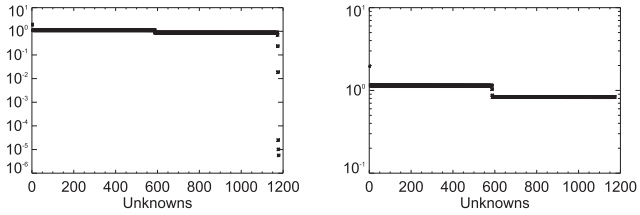

Fig. 9. (Left) Singular value spectrum of overdetermined forward operator. The condition number of the problem is of the order of magnitude of 10^5. (Right) Singular value spectrum of underdetermined forward operator. In this case, the condition number is around 2.

a constant offset [27], [28], should be adapted to consider the equivalent θ_c-dependent baseline error transferred from the repeat-pass data [second term of (6)].

Although the equivalent single-pass error model is simple, it corresponds to a poorly conditioned estimation problem due to the lack of diversity of the incidence-dependent terms along the valid swath. This is verified in the simulation results presented in Fig. 8, which shows the resulting maximum height error due to miscalibration as a function of the employed number of reference points. For the simulation, an X-band single-pass phase was synthesized considering different constant standard deviation values ranging from 1° to 35°. The topography information provided by the reference points is assumed to be error free; hence, all the error is due to phase noise or residual multipath artifacts in the SAR image. The results show that, even for a standard deviation of 5°, more than 10 points are necessary for a robust estimation, effectively impeding the calibration using GCP. Given that an accurate reference DEM is not necessarily available for the correction, an alternative is to resort to the multifrequency information in order to separate the multipath components from the baseline error. Specifically, we exploit the difference between the single-pass residual phases

$$\phi_{\text{diff}}^{\text{SX}}(\theta_c) = \phi_{\text{mp}}^{\text{S}_{\text{SP}}}(\theta_c) - \frac{k_{z,\text{real}}^{\text{S}_{\text{SP}}}}{k_{z,\text{real}}^{\text{X}_{\text{SP}}}}(\theta_c)\phi_{\text{mp}}^{\text{X}_{\text{SP}}}(\theta_c). \tag{7}$$

The error model in (6) and (7) can be combined in a linear system of equations in the form of

$$\boldsymbol{A}y = B_{\text{obs}} \tag{8}$$

with

$$y = \left[\phi_{\text{mp}}^{\text{X}_{\text{SP}}}(\Theta) \quad \phi_{\text{mp}}^{\text{S}_{\text{SP}}}(\Theta) \quad \varepsilon_y^{\text{X}_{\text{RP}}} \quad \varepsilon_z^{\text{X}_{\text{RP}}} \quad \varepsilon_y^{\text{S}_{\text{RP}}} \quad \varepsilon_z^{\text{S}_{\text{RP}}} \quad \nu_{\text{X}} \quad \nu_{\text{S}}\right]^T \tag{9}$$

where $\Theta = [\theta_{c,1} \cdots \theta_{c,P}]$ is the common incidence angle vector. From (9), the total number of unknowns is $(2P + 6)$, while the observation vector

$$B_{\text{obs}} = \left[\phi_{\text{diff}}^{\text{X}}(\Theta) \quad \phi_{\text{diff}}^{\text{S}}(\Theta) \quad \phi_{\text{diff}}^{\text{SX}}(\Theta)\right]^T \tag{10}$$

comprises $3P$ elements. If $P > 6$, the system in (8) is overdetermined. However, the singular value spectrum seen in Fig. 9 (left) shows that the last three singular values are small, indicating a poorly conditioned problem [68]. Hence, small errors in the observation vector may hinder the separation of the multipath phase profile from the equivalent baseline errors, and a regularization strategy should be considered, e.g., by means of truncated singular value decomposition [69]. Alternatively, we suggest to directly employ the truncated problem defined by

$$\boldsymbol{A}_{\text{trunc}}y_{\text{trunc}} = B_{\text{obs,trunc}} \tag{11}$$

where the forward operator $\boldsymbol{A}_{\text{trunc}}$ is constructed from (6) and (7)

$$B_{\text{obs,trunc}} = \left[\phi_{\text{diff}}^{\text{X}}(\Theta) \quad \phi_{\text{diff}}^{\text{SX}}(\Theta)\right]^T \tag{12}$$

and

$$y_{\text{trunc}} = \left[\phi_{\text{mp}}^{\text{X}_{\text{SP}}}(\Theta) \quad \phi_{\text{mp}}^{\text{S}_{\text{SP}}}(\Theta) \quad \varepsilon_y^{\text{X}_{\text{RP}}} \quad \varepsilon_z^{\text{X}_{\text{RP}}} \quad \nu_{\text{X}}\right]^T. \tag{13}$$

The singular value spectrum of the truncated forward operator is shown in Fig. 9 (right) and confirms its better conditioning. The minimization is solved with a least-norm approach, that is

$$\min \|y_{\text{trunc}}\|_2 \quad \text{s.t. } \boldsymbol{A}_{\text{trunc}}y_{\text{trunc}} = B_{\text{obs,trunc}} \tag{14}$$

typically used for underdetermined problems. Note that the model is able to retrieve the individual multipath profiles up to a constant offset, since the separability between the offsets in the X- and S-band phase profiles depends on the variation along the range of $k_{z,\text{real}}^{\text{S}_{\text{SP}}}/k_{z,\text{real}}^{\text{X}_{\text{SP}}}$, which is usually small. As a consequence, the calibration of a phase offset in a posterior step is required. Moreover, if the unknown offsets are large, the least-norm optimization gives poorer results. Hence, a rough estimation of the offset should be performed based on the mean terrain information and subtracted from the phases beforehand.

E. Validation With Simulated and Real Data

The approach was validated with simulations using synthesized phases considering a gentle slope varying from 18 to 25 m as the true terrain information. Phase standard deviations of 5° and 10° were considered for single- and repeat-pass phases. The low standard deviation value is consistent with the empirical observations and is justified by the fact that the estimation is performed over the averaged profiles, as previously discussed. In addition to the topographic information and noise, the single-pass phases contain the multipath artifacts generated from the reflection model. On the other hand, the repeat-pass phases comprise artifacts due to constant

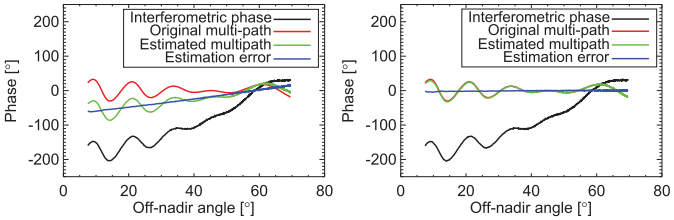

Fig. 10. Black curves: simulated interferometric phase profile. Red curves: simulated X-band multipath phase profile. Green curves: estimated profiles. Blue curves: estimation error. (Left) Overdetermined model was considered, failing to estimate the multipath profile. (Right) Model (14) was used and the estimation error is under 2°.

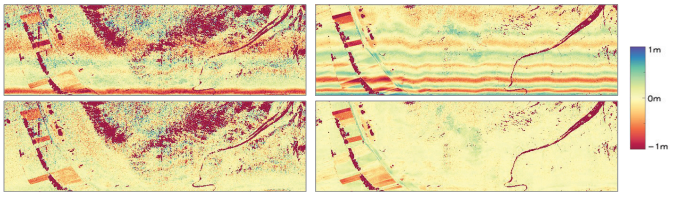

Fig. 11. Differences between the reference ALS DEM and the obtained (Left) S-band and (Right) X-band elevation models for a block of F-SAR DFDB data. (Top row) No multipath mitigation was applied. (Bottom row) Proposed DFDB multipath mitigation strategy was employed to correct the phase undulations. The data correspond to the first third of the scene, and a block of 256 samples in its center was used to estimate the multipath profile.

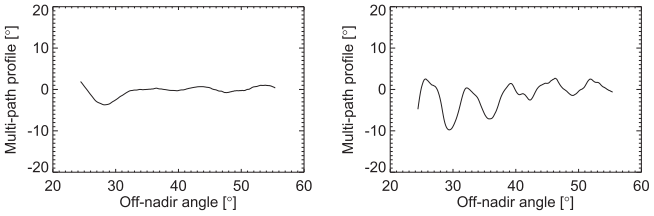

Fig. 12. (Left) Estimated S-band multipath profile. (Right) Estimated X-band multipath profile.

baseline errors. The simulation results are shown in Fig. 10. The black curves show the phase difference between simulated X-band repeat- and single-pass interferograms, the red ones show the simulated X-band multipath phase profile, the green curves are the estimated profiles, and finally, the blue curves show the estimation error. In Fig. 10 (left), the overdetermined model was considered, which failed to separate the multipath profile from the baseline errors. In Fig. 10 (right), the truncated problem was considered providing a much better estimation (errors less than 2°).

Finally, real F-SAR DFDB data are considered. The block of data corresponds to the first third of the acquisition, which is described in detail in Section X. Fig. 11 shows the height difference between a reference ALS DEM and the obtained (left) S- and (right) X-band F-SAR single-pass elevation models. The results in the first row correspond to the case when no multipath mitigation is applied, and the errors up to 1 m are observed in both S- and X-band differences. The results in the second row were obtained after applying the proposed DFDB multipath mitigation strategy, and the range phase undulations are no longer visible. Fig. 12 shows the

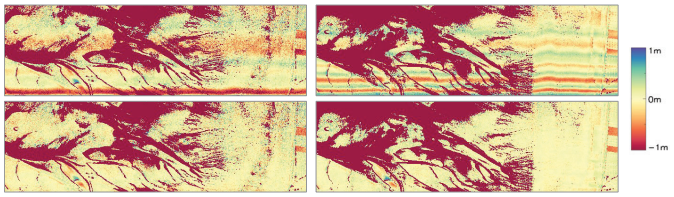

Fig. 13. Differences between the reference ALS DEM and the obtained (Left) S-band and (Right) X-band elevation models for a block of F-SAR DFDB data. (Top row) No multipath mitigation was applied. (Bottom row) Proposed DFDB multipath mitigation strategy was employed to correct the phase undulations. The data correspond to the last third of the scene.

estimated multipath profiles for (left) S-band data and (right) X-band data. The profiles were estimated using 256 samples located around the center of the data block shown in Fig. 11, and was then interpolated accounting for the incidence angle and attitude variations in order to provide a 2-D correction for the whole scene. The robustness of the estimation can be appreciated in Fig. 13, which also shows the height differences between F-SAR and ALS reference (top) before and (bottom) after the mitigation of multipath artifacts, but now for the final third of the scene. As in Fig. 11, the range undulations are no longer visible.

Up to this point, it is assumed that the incidence angle information is accurate, which is not the case if the topography is not known. Usually, a low accuracy reference elevation model is employed during the image processing, and can be used for the initial estimation of θ and $k_{z,\text{real}}^{*}$. The effect of the unknown topography should be small for flat terrains, and, in general, can be compensated by using an iterative estimation approach. For this purpose, after the correction and baseline calibration, the single-pass phase is transformed to height and used for the better assessment of θ. The multipath profile can then be reestimated, and θ_c with finer sampling can be used to estimate higher frequency components. The process can be repeated until the changes in the incidence angle are negligible, but, normally, two iterations suffice. Note that the multipath mitigation process can be performed using undersampled phases due to the low-pass characteristics of both multipath phase profile and baseline errors, such that the computational burden of the whole estimation process is affordable.

VI. Baseline Errors and Phase Offset Calibration

Considering that proper internal calibration and coregistration procedures were performed during the processing of the single-look complex images [43], the single-pass phases should not contain fringes due to linear or constant baseline errors. Nevertheless, they might enclose an unknown offset due to, e.g., inaccurate range delay estimation or the lack of absolute referencing of the phase unwrapping. Moreover, an offset might be introduced by the multipath mitigation strategy, as discussed in Section V. On the other hand, the repeat-pass phases might be affected by constant and linearly varying baseline errors and a global phase offset, as described in Section V [54].

A. General Calibration Approach

Here, we propose to estimate the repeat- and single-pass constant and linear phase errors jointly without the use of external references. In this case, the unknown topography is accounted for by considering the differences between the available single- and repeat-pass phases, that is

$$\phi_{\text{diff}}^{\text{X,S}} = k_{\text{X,S}} \cdot \phi_{\text{res}}^{\{\text{X,S}\}_{\text{SP}}} - \phi_{\text{res}}^{\{\text{X,S}\}_{\text{RP}}} \tag{15}$$

where

$$k_{\text{X,S}} = \frac{k_{z,\text{real}}^{\{\text{X,S}\}_{\text{RP}}}}{k_{z,\text{real}}^{\{\text{X,S}\}_{\text{SP}}}}. \tag{16}$$

In general, the estimation of the unknowns of the baseline error model described by (5) can be performed individually for the data of each frequency of acquisition. However, airborne repeat-pass interferometric phases are often affected by higher order spatially correlated errors not accounted for in this model. Depending on the characteristics of such errors and on the quality of the interferometric phases, a simple model-based least-squares (LS) solution considering independently each frequency of acquisition may be biased. In fact, the baseline calibration problem can be more robustly defined exploring the correlation between higher order artifacts in X- and S-band phases, benefiting from the simultaneous acquisition of the data sets. In this case, a multiobjective optimization problem is considered

$$\begin{aligned}\underset{y_{\text{X}}, y_{\text{S}}, y_{\text{XS}}}{\arg\min} \; & \| \boldsymbol{A}_{\mathbf{X}} y_{\text{X}} - \hat{\phi}_{\text{diff}}^{\text{X}} \|^2 \\ & + \mu_1 \| \boldsymbol{A}_{\mathbf{S}} y_{\text{S}} - \hat{\phi}_{\text{diff}}^{\text{S}} \|^2 + \mu_2 \| \boldsymbol{A}_{\mathbf{XS}} y_{\text{XS}} - \hat{\phi}_{\text{diff}}^{\text{XS}} \|^2 \end{aligned} \tag{17}$$

where

$$y_{\text{XS}} = \left[\varepsilon_{y_1}^{\text{S}} \; \varepsilon_{y_2}^{\text{S}} \; \varepsilon_{z_1}^{\text{S}} \; \varepsilon_{z_2}^{\text{S}} \; \varepsilon_{y_1}^{\text{X}} \; \varepsilon_{y_2}^{\text{X}} \; \varepsilon_{z_1}^{\text{X}} \; \varepsilon_{z_2}^{\text{X}} \; \nu_{\text{S}_{\text{RP}}} \; \nu_{\text{X}_{\text{RP}}}\right]^T \tag{18}$$

$\hat{\phi}_{\text{diff}}^{\text{XS}}$ is the observation of the difference between the X- and S-band repeat-pass phases

$$\phi_{\text{diff}}^{\text{XS}} \approx \phi_{\text{res}}^{\text{X}_{\text{RP}}} - \frac{\lambda_{\text{S}}}{\lambda_{\text{X}}} \phi_{\text{res}}^{\text{S}_{\text{RP}}} \tag{19}$$

and the forward operators $\boldsymbol{A}_{*}$ are constructed according to the model in (5).

The parameters $\mu_1 \geqslant 0$ and $\mu_2 \geqslant 0$ in (17) are used to ensure proper scaling of the objectives and to provide relative weightings between the minimization of DFDB differences, allowing larger errors in the former. If $\mu_2 = 0$, the solution is equivalent to individually calibrating X- and S-band data sets.

B. Simplification for Simultaneous Acquisitions

Since in the proposed DFDB configuration, X- and S-band data are simultaneously acquired, and considering that after a proper lever-arms calibration, the absolute positions of the phase centers are known, we can assume that constant and linearly varying baseline errors are the same in X- and S-band repeat-pass data (i.e., $\varepsilon_{z_*}^{\text{S}} = \varepsilon_{z_*}^{\text{X}} = \varepsilon_{z_*}$ and $\varepsilon_{y_*}^{\text{S}} = \varepsilon_{y_*}^{\text{X}} = \varepsilon_{y_*}$). Hence, (17) can be expressed in the following equivalent LS optimization:

$$\underset{y_{\text{eq}}}{\arg\min} \; \| \boldsymbol{A}_{\mathbf{eq}} y_{\text{eq}} - \hat{\phi}_{\text{diff}} \|^2 \tag{20}$$

where

$$\mathbf{A_{eq}} = \begin{bmatrix} -\frac{4\pi}{\lambda_{\text{X}}} \sin\boldsymbol{\Theta} & -\mu_1 \frac{4\pi}{\lambda_{\text{S}}} \sin\boldsymbol{\Theta} & \mathbf{0} \\ -\frac{4\pi}{\lambda_{\text{X}}} \boldsymbol{x} \sin\boldsymbol{\Theta} & -\mu_1 \frac{4\pi}{\lambda_{\text{S}}} \boldsymbol{x} \sin\boldsymbol{\Theta} & \mathbf{0} \\ -\frac{4\pi}{\lambda_{\text{X}}} \cos\boldsymbol{\Theta} & -\mu_1 \frac{4\pi}{\lambda_{\text{S}}} \cos\boldsymbol{\Theta} & \mathbf{0} \\ -\frac{4\pi}{\lambda_{\text{X}}} \boldsymbol{x} \cos\boldsymbol{\Theta} & -\mu_1 \frac{4\pi}{\lambda_{\text{S}}} \boldsymbol{x} \cos\boldsymbol{\Theta} & \mathbf{0} \\ -\mathbf{1} & \mathbf{0} & \mu_2 \mathbf{1} \\ \mathbf{0} & -\mathbf{1} & -\mu_2 \frac{\lambda_{\text{S}}}{\lambda_{\text{X}}} \mathbf{1} \\ k_{\text{X}}(\boldsymbol{\Theta}) & \mathbf{0} & \mathbf{0} \\ \mathbf{0} & \mu_1 k_{\text{S}}(\boldsymbol{\Theta}) & \mathbf{0} \end{bmatrix}^T \tag{21}$$

$$y_{\text{eq}} = [\varepsilon_{y_1} \; \varepsilon_{y_2} \; \varepsilon_{z_1} \; \varepsilon_{z_2} \; \nu_{\text{X}_{\text{RP}}} \; \nu_{\text{S}_{\text{RP}}} \; \nu_{\text{X}_{\text{SP}}} \; \nu_{\text{S}_{\text{SP}}}]^T \tag{22}$$

and

$$\hat{\phi}_{\text{diff}} = \left[\hat{\phi}_{\text{diff}}^{\text{X}} \quad \mu_1 \hat{\phi}_{\text{diff}}^{\text{S}} \quad \mu_2 \hat{\phi}_{\text{diff}}^{\text{XS}}\right]^T. \tag{23}$$

Given the accuracy of the measuring instruments, it is reasonable to expect that the baseline errors are small. Hence, a mixed LS optimization can be employed regularizing the solution

$$\begin{aligned} \underset{y_{\text{eq}}}{\arg\min} \; & \| \boldsymbol{A}_{\mathbf{eq}} y_{\text{eq}} - \hat{\phi}_{\text{diff}} \|^2 \\ \text{s.t.} \; & \| y_{\text{be}} \| \leq \delta \end{aligned} \tag{24}$$

where y_{be} is a subvector of y_{eq} corresponding to the baseline errors only, i.e., the first four terms of (22), and the vector δ gives their magnitude thresholds.

C. Extension to the Complex Domain

Up to now, unwrapping errors have been neglected. If those are indeed present, the LS optimizations in (24) will be biased. Moreover, at least a relative calibration between the X- and S-phases is required before unwrapping, requiring an approach suitable for wrapped phases. In the following, we propose a complex domain alternative based on the estimation of local phase slopes [70], [71]. The dual-frequency approach based on the forward operator in (21) is considered, but the adaptation to the single-frequency, or, more generally, the single-channel case, is straightforward.

For the derivation, the complex signals obtained from the noiseless phase differences $\phi_{\text{diff}}^{\text{X}}$ and $\phi_{\text{diff}}^{\text{S}}$ are locally (i.e., blockwise) modeled in terms of 2-D complex sine waves

$$s_{\text{diff}}^{\text{X,S}}(r, x) = \exp\left[j\left(f_r^{\text{X,S}} r + f_x^{\text{X,S}} x\right)\right] \tag{25}$$

where $-N_r/2 \leqslant r \leqslant N_r/2$ and $-N_x/2 \leqslant x \leqslant N_x/2$ are the pixel coordinates within a window of size N_r x N_x; and f_r^* and f_x^* are the local spatial slopes along the range and azimuth directions and correspond to the derivatives of the expected

phase along the range and azimuth directions sampled at the window center position. The new optimization problem is

$$\arg\min_{y_c} \left\| \begin{bmatrix} \boldsymbol{A_r} \\ \boldsymbol{A_x} \end{bmatrix} y_c - \begin{bmatrix} \hat{F}_r \\ \hat{F}_x \end{bmatrix} \right\|^2 \tag{26}$$

where

$$\boldsymbol{A_r} = \begin{bmatrix} -\frac{4\pi \cos \boldsymbol{\Theta}}{\lambda_{\mathrm{X}} \boldsymbol{r} \tan \boldsymbol{\Theta}} & -\frac{4\pi \cos \boldsymbol{\Theta}}{\lambda_{\mathrm{S}} \boldsymbol{r} \tan \boldsymbol{\Theta}} \\ -\frac{4\pi \mathbf{x} \cos \boldsymbol{\Theta}}{\lambda_{\mathrm{X}} \boldsymbol{r} \tan \boldsymbol{\Theta}} & -\frac{4\pi \mathbf{x} \cos \boldsymbol{\Theta}}{\lambda_{\mathrm{S}} \boldsymbol{r} \tan \boldsymbol{\Theta}} \\ \frac{4\pi}{\lambda_{\mathrm{X}} \boldsymbol{r} \cos \boldsymbol{\Theta}} & \frac{4\pi}{\lambda_{\mathrm{S}} \boldsymbol{r} \cos \boldsymbol{\Theta}} \\ \frac{4\pi \mathbf{x}}{\lambda_{\mathrm{X}} \boldsymbol{r} \cos \boldsymbol{\Theta}} & \frac{4\pi \mathbf{x}}{\lambda_{\mathrm{S}} \boldsymbol{r} \cos \boldsymbol{\Theta}} \\ \frac{\partial k_{\mathrm{X}}}{\partial \boldsymbol{\Theta}} \frac{1}{\boldsymbol{r} \tan \boldsymbol{\Theta}} & \mathbf{0} \\ \mathbf{0} & \frac{\partial k_{\mathrm{S}}}{\partial \boldsymbol{\Theta}} \frac{1}{\boldsymbol{r} \tan \boldsymbol{\Theta}} \end{bmatrix}^T \tag{27}$$

with

$$\frac{\partial k_{\mathrm{X,S}}}{\partial \boldsymbol{\Theta}} = \frac{B_{\{\mathrm{X,S}\}_{\mathrm{RP}}}}{B_{\{\mathrm{X,S}\}_{\mathrm{SP}}}} \frac{\sin(\alpha_{\mathrm{RP}} - \alpha_{\mathrm{SP}})}{\cos^2(\boldsymbol{\Theta} - \alpha_{\mathrm{SP}})} \tag{28}$$

$$\boldsymbol{A_x} = \begin{bmatrix} \mathbf{0} & \mathbf{0} \\ -\frac{4\pi}{\lambda_{\mathrm{X}}} \sin \boldsymbol{\Theta} & -\frac{4\pi}{\lambda_{\mathrm{S}}} \sin \boldsymbol{\Theta} \\ \mathbf{0} & \mathbf{0} \\ -\frac{4\pi}{\lambda_{\mathrm{X}}} \cos \boldsymbol{\Theta} & -\frac{4\pi}{\lambda_{\mathrm{S}}} \cos \boldsymbol{\Theta} \\ \frac{\partial k_{\mathrm{X}}}{\partial \boldsymbol{x}} & \mathbf{0} \\ \mathbf{0} & \frac{\partial k_{\mathrm{S}}}{\partial \boldsymbol{x}} \end{bmatrix}^T \tag{29}$$

with

$$\frac{\partial k_{\mathrm{X,S}}}{\partial \boldsymbol{x}} = \frac{B_{\{\mathrm{X,S}\}_{\mathrm{SP}}} \frac{\partial B_{\{\mathrm{X,S}\}_{\mathrm{RP}}}}{\partial \boldsymbol{x}} - B_{\{\mathrm{X,S}\}_{\mathrm{RP}}} \frac{\partial B_{\{\mathrm{X,S}\}_{\mathrm{SP}}}}{\partial \boldsymbol{x}}}{B^2_{\{\mathrm{X,S}\}_{\mathrm{SP}}}} \cdot \frac{\cos(\boldsymbol{\Theta} - \alpha_{\mathrm{RP}})}{\cos(\boldsymbol{\Theta} - \alpha_{\mathrm{SP}})} \tag{30}$$

$$y_c = \begin{bmatrix} \varepsilon_{y_1} & \varepsilon_{y_2} & \varepsilon_{z_1} & \varepsilon_{z_2} & \nu_{\mathrm{X_{SP}}} & \nu_{\mathrm{S_{SP}}} \end{bmatrix}^T \tag{31}$$

$$\hat{F}_r = \begin{bmatrix} \hat{f}_{\boldsymbol{r}}^{\mathrm{X}} & \hat{f}_{\boldsymbol{r}}^{\mathrm{S}} \end{bmatrix} \tag{32}$$

and

$$\hat{F}_x = \begin{bmatrix} \hat{f}_{\boldsymbol{x}}^{\mathrm{X}} & \hat{f}_{\boldsymbol{x}}^{\mathrm{S}} \end{bmatrix}. \tag{33}$$

The vectors $\boldsymbol{\Theta}$ and $\boldsymbol{r}$ contain the incidence angle and range position at the center of each block in the first dimension, whereas $\boldsymbol{x}$ contains the azimuth position at the center of the block in the second dimension. A simple way to obtain the components of the observation vectors $\hat{F}_{r,x}$ is by locating the position of maximum amplitude of the Fourier transform of each considered block.

Given the nature of the modeling, the constant offsets of the repeat-pass phases cannot be estimated using the local slopes. As a consequence, after performing the optimization in (26) and compensating for the obtained phase error, the offsets of the repeat-pass phases have to be estimated using the single-pass phases as references. To mitigate the effect of unwrapping errors, the offsets can be calculated by evaluating the maximum of the histograms of the phase differences.

TABLE I
SIMULATED BASELINE ERRORS

	First Simulation	Second Simulation	Third Simulation
ε_{y_1}	27.0 mm	7.5 mm	50.0 mm
ε_{y_2}	1.8 mm	0.5 mm	10 mm
ε_{z_1}	42.0 mm	11.0 mm	50.0 mm
ε_{z_2}	0.2 mm	0.0 mm	1.0 mm

Although the above-discussed complex domain approach has the advantage of allowing for a linear LS optimization, the accuracy of the estimation is limited by the resolution of the Fourier transform and the validity of the 2-D complex sine wave model itself. In order to refine the result, the complex error model can be used within a nonlinear LS framework, i.e., the solution is found through

$$\arg\min_{y_c} \left\| e^{j \boldsymbol{A_{\mathrm{eq}}} y_{\mathrm{eq}}} - e^{j \hat{\phi}_{\mathrm{diff},c}} \right\|^2 \tag{34}$$

where

$$\hat{\phi}_{\mathrm{diff},c} = \begin{bmatrix} \hat{\phi}_{\mathrm{diff}}^{\mathrm{X}} + \hat{\nu}_{\mathrm{X_{RP,0}}} \\ \mu_1 \left(\hat{\phi}_{\mathrm{diff}}^{\mathrm{S}} + \hat{\nu}_{\mathrm{S_{RP,0}}} \right) \\ \mu_2 \left(\hat{\phi}_{\mathrm{diff}}^{\mathrm{XS}} - \hat{\nu}_{\mathrm{X_{RP,0}}} + \frac{\lambda_{\mathrm{S}}}{\lambda_{\mathrm{X}}} \hat{\nu}_{\mathrm{S_{RP,0}}} \right) \end{bmatrix} \tag{35}$$

with $\mathbf{A}_{\mathrm{eq}}$ and y_{eq} as in (21) and (22), and where $\hat{\nu}_{*\mathrm{RP},0}$ are the initial estimates of the constant phase offsets. The optimization in (34) can be solved using the iterative Levenberg–Marquardt algorithm [72] with an initial solution obtained through (26).

Note that the computation of $\hat{\phi}_{\mathrm{diff}}^{\mathrm{XS}}$ for (35) requires the scaling of the S-band repeat-pass phase. If this phase contains unwrapping errors, those can bias the estimation depending on how large the remainder of $\lambda_{\mathrm{S}}/\lambda_{\mathrm{X}}$ is and on how large the 2π ambiguities are. However, if the ratio between the wavelengths is close to an integer, as in the F-SAR X- and S-band configuration ($\lambda_{\mathrm{S}}/\lambda_{\mathrm{X}} \approx 3.01$), the baseline calibration can still profit from the joint dual-frequency estimation even in the presence of small residual unwrapping errors.

Finally, note that the extension of the two-step complex domain calibration approach to consider the more general calibration model described by (17) is straightforward. This could be used, for example, when two repeat-pass data sets independently acquired are available instead of data from two acquisition frequencies.

D. Validation With Simulated and Real Data

Fig. 14 shows the results from Monte Carlo simulations performed in order to evaluate the convergence of the proposed baseline calibration algorithm. Two sets of parameters were chosen in accordance to typical observations from F-SAR interferometric processing, and are shown in the second and third columns of Table I ("First Simulation" and "Second Simulation"). The noisy interferometric phases were simulated considering a flat terrain and a constant coherence value of 0.6. Two optimization schemes were considered: the DFDB problem represented by (34) [see Fig. 14 (left)] and the single-frequency problem, where S- and X-band phases were

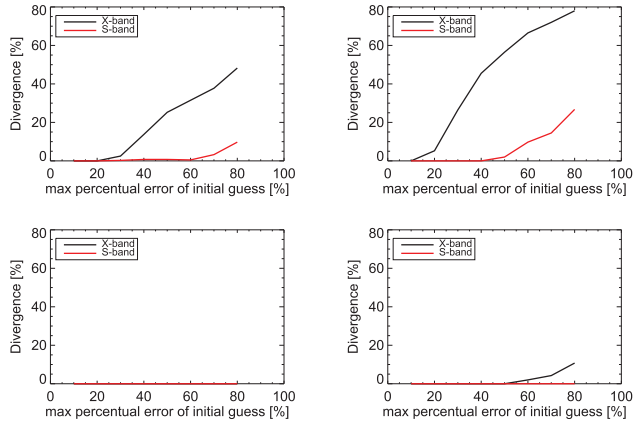

Fig. 14. Results from Monte Carlo simulations showing the failure rate according to the maximum allowed error in the initial estimation. Failure is defined here as the percentage of cases for which the error in the retrieved parameters causes an interferometric phase error larger than 3°. (Left) Results for the proposed dual-frequency scheme. (Right) Results for the single channel case. (Top) Nominal baseline error for this simulation can be found in the second column of Table I, identified as "First Simulation." (Bottom) Nominal baseline error can be found in the third column of Table I, identified as "Second Simulation."

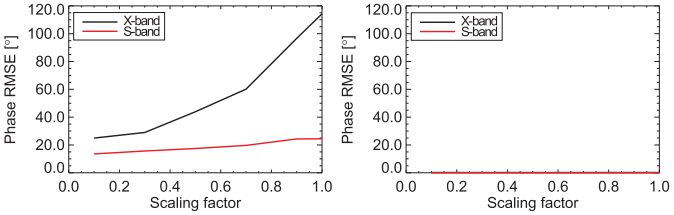

Fig. 15. Results from Monte Carlo simulations showing (Left) performance of the estimation based on the local slopes only and (Right) performance of the two-step strategy. The performance is evaluated in terms of the phase RMSE introduced by the estimation error as a function of the scaling factor, i.e., as a function of the magnitude of the nominal baseline errors.

Fig. 16. Rewrapped difference between the X- and S-band phases after calibration (phases scaled to the S-band geometry). (Top) Data set of each acquisition frequency was individually calibrated. (Bottom) DFDB scheme was employed.

individually calibrated [see Fig. 14 (right)]. The initial solution used for the complex optimization was randomly sampled from a uniform distribution, such that the maximum allowed error for any parameter is a percentage of the nominal value. The results show the failure rate according to the maximum allowed error, where "failure" is defined as the percentage of cases for which the error in the retrieved parameters causes an interferometric phase error larger than 3°. In both simulations, it is possible to see the convergence improvement due to the use of the dual-frequency information in comparison with the single channel case.

A slightly different simulation is performed to evaluate the convergence of the complete scheme, i.e., initial estimation with the slope model, followed by refinement with the nonlinear LS optimization. For the simulation, nominal baseline errors are randomly sampled in the interval

$$y_c \in \left[0.9 \cdot a \cdot y_{c,3},\, 1.1 \cdot a \cdot y_{c,3}\right], \quad a \in [0,\, 1] \tag{36}$$

where a is scaling factor and the components of $y_{c,3}$ are given in the fourth column of Table I ("Third Simulation"). The variation of the phase root-mean-square error (RMSE) caused by the baseline estimation error as a function of the scaling factor is shown in Fig. 15. Fig. 15 (left) shows the error using the slope model alone, i.e., using only the initial estimation, while Fig. 15 (right) shows the result using the two-step strategy. Note that even for the larger errors in the initial estimation, the estimation provided by the slope-based model is sufficient to ensure the convergence of the nonlinear LS. Moreover, using the refined estimation, the performance is improved for both the X- and S-band cases. Given its better performance, the two-step strategy is employed for the calibration of the DFDB data set and its effectiveness can be appreciated in the comparison between the obtained SAR DEMs and the ALS reference, as shown in Section X (see Fig. 30).

A final validation is given in Fig. 16, where the difference between the X- and S-band repeat-pass phases after the calibration is shown. In Fig. 16 (top and bottom), the data sets were calibrated with the complex domain scheme. However, for the result shown at the top, the data sets from the X- and S-band were individually calibrated, whereas for the result at the bottom, the dual-frequency estimation was employed. The phases are scaled to the S-band geometry, and to avoid misinterpretation due to unwrapping errors, the phase differences are rewrapped and a water mask has been applied. Fig. 16 (top) indicates that the calibration of the phases considering the single-frequency model diverged due to the presence of unmodeled low-frequency artifacts, leading to a phase trend in the azimuth (horizontal) direction. Consequently, the difference between the X- and S-band phases diverges, and phase fringes are observed. On the other hand, the more robust dual-frequency model provides consistent results.

VII. Unwrapping Errors' Correction

Although multichannel algorithms like the one in [36] promote a successful phase unwrapping, the ill-posed nature of the unwrapping problem can still cause residual errors. A typical challenging case is when large incoherent areas cross the whole swath, e.g., due to the presence of flooded areas or forests in the scene, potentially leading to large-scale unwrapping errors [24], [36], [44].

We tackle the unwrapping error detection as a classification problem, i.e., the phases are segmented into regions corresponding to an integer multiple of 2π. The procedure is divided in two steps: 1) the generation of an initial classification map using the DFDB phase differences and 2) the refinement of the solution by means of an active-contour-based algorithm. According to the estimated classification maps, the proper 2π multiples are compensated.

At this point of the chain, the residual phases can be modeled as

$$\phi_{\text{res}}^{\text{X}_{\text{SP}},\text{S}_{\text{SP}},\text{X}_{\text{RP}},\text{S}_{\text{RP}}} = k_{z,\text{real}}^{\text{X}_{\text{SP}},\text{S}_{\text{SP}},\text{X}_{\text{RP}},\text{S}_{\text{RP}}} \Delta h + n_{\text{err}}^{\text{X}_{\text{SP}},\text{S}_{\text{SP}},\text{X}_{\text{RP}},\text{S}_{\text{RP}}} 2\pi + \varepsilon^{\text{X}_{\text{SP}},\text{S}_{\text{SP}},\text{X}_{\text{RP}},\text{S}_{\text{RP}}} \tag{37}$$

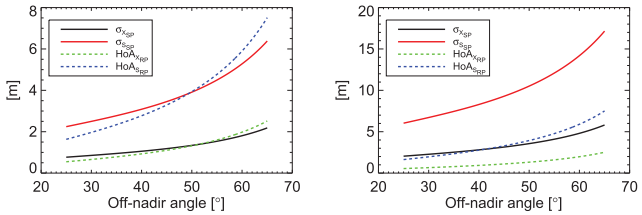

Fig. 17. Expected standard deviation of the noise in the height maps generated with the single-pass data (black curve corresponds to X-band and red curve corresponds to S-band) and the HoA of the repeat-pass data (green curve corresponds to X-band and blue curve corresponds to S-band). (Left) Single-pass coherence value of 0.9 was considered. (Right) Value was 0.6.

where Δh is the unknown height increment in relation to the used reference height (e.g., mean terrain value or reference DEM), n^*_{err} are the ambiguity errors, and ε^* are phase errors unrelated with the unwrapping, e.g., noise and low-frequency artifacts.

The HoA of the single-pass data sets is usually large enough to allow for a reliable phase unwrapping, especially if the proposed dual-channel approach is employed. In fact, even if unwrapping errors occur, they can be identified and corrected, assuming that the residual topographic phase and other errors are not big enough to modify the ambiguity error, that is

$$k_{z,\text{real}}^{\{\text{X,S}\}\text{SP}}\Delta h + \varepsilon^{\{\text{X,S}\}\text{SP}} \ll \pi \tag{38}$$

in which case, unwrapping errors can be found by simply calculating the nearest integer

$$n_{\text{err}}^{\{\text{X,S}\}\text{SP}} = \left\lfloor \frac{\phi_{\text{res}}^{\{\text{X,S}\}\text{SP}}}{2\pi} \right\rceil. \tag{39}$$

Hence, $n^{\text{X}_{\text{SP}}}$ and $n^{\text{S}_{\text{SP}}}$ are neglected in the following argumentation, which focuses on the more challenging identification of unwrapping errors in the repeat-pass scenario. The initial segmentation maps of the X- and S-band repeat-pass phases are estimated as

$$I_{\text{X,S}} = \left\lfloor \frac{\phi_{\text{res}}^{\{\text{X,S}\}\text{RP}} - \frac{k_{z,\text{real}}^{\{\text{X,S}\}\text{RP}}}{k_{z,\text{real}}^{\{\text{X,S}\}\text{SP}}}\phi_{\text{res}}^{\{\text{X,S}\}\text{SP}}}{2\pi} \right\rceil. \tag{40}$$

Due to the large-baseline ratio between the considered single- and repeat-pass interferometers, the classification maps obtained through (40) can be very noisy. For example, the simulation results in Fig. 17 show the expected noise standard deviation after phase-to-height conversion for the S-band and X-band single-pass data, together with the HoA of the repeat-pass data sets. An effective repeat-pass baseline of around 30 m and the single-pass coherences of 0.9 (left) and 0.6 (right) were considered for the simulation. In both cases, the repeat-pass HoA is of the same order as the noise standard deviation in the single-pass height map of the same frequency, leading to misclassification.

Low-frequency phase biases in the repeat-pass interferograms further deteriorate the classification maps in (40). Although the difference between the repeat-pass phases can aid in the detection of unwrapping failure, it cannot provide an unambiguous measure of the unwrapping errors unless they are known to be present only in one of the data sets. Moreover, in cases where

$$n_{\text{err}}^{\text{S}_{\text{RP}}} \approx \frac{k_{z,\text{real}}^{S_{\text{RP}}}}{k_{z,\text{real}}^{\text{X}_{\text{RP}}}} n_{\text{err}}^{\text{X}_{\text{RP}}} \tag{41}$$

typical when close-to-integer wavelengths ratios are employed, the difference between the repeat-pass phases provides little help to the detection of errors. Nevertheless, it can be used as an indicator of miscalculation of the ambiguity numbers through (40), since in this case, the difference between the corrected repeat-pass phases tend to increase.

Similar to the suggested scheme for the baseline errors calibration in Section VI, we proposed here to jointly use all available data sets for the unwrapping errors detection, thus mitigating the effect of phase biases in the repeat-pass interferograms. Moreover, a regularized active-contour-based solution is proposed in order to cope with noise scaling while respecting the borders of large-scale unwrapping errors.

Active contours and variational calculus are the common tools for the detection of object boundaries in image processing applications, and have been widely used in the context of edge detection and image segmentation [73]–[78]. The contours are defined in the image domain and are either attracted or repelled by external forces, finally converging to the location of feature boundaries. The design of such forces will ultimately define the characteristics of the detected objects or the final segmentation map.

In the SAR context, active contours have been mainly used for image segmentation, e.g., in [79], where a statistical model based on the estimation of local tone and texture was proposed to guide the curve evolution along the classical tension and stiffness constraints. In [80], a multiregion level-set model able to segment SAR images in an arbitrary number of homogeneous regions was introduced, and later expanded to consider polarimetric images [81]. Silveira and Heleno [82] introduced a statistical model based on a mixture of log-normal densities to perform water/land segmentation in SAR images. A few studies investigated the use of active contours in InSAR: [83] proposed a user-dependent method to extract the contour map that characterizes the interferometric fringes followed by a block integration to perform the phase unwrapping and [84] introduced different functionals to support the phase estimation and unwrapping.

The approach suggested in the following focuses on the identification and correction of residual unwrapping errors rather than the detection of interferometric phase fringes. For this purpose, the multiphase evolution scheme proposed in [75] for image classification is adapted to the InSAR DFDB scenario. For completion, a summary of the algorithm in [75] is given in the following, followed by the adaptation to the unwrapping errors correction scenario.

A. Review of Active Contours for Image Segmentation

The method in [75] intends to segment an image into K classes, each one characterized by a certain mean and standard deviation. Formally, being Ω an open connected

subspace of $\mathbb{R}^2$, its partition P is defined as the set $\{\Omega_i\}_{i=1\ldots K}$, such as

$$\begin{aligned} \emptyset &\notin P \\ \Omega &= \bigcup_{i=1}^{K} \Omega_i \\ \Omega_i &\bigcap_{i\neq j} \Omega_j = \emptyset \end{aligned} \tag{42}$$

where $\emptyset$ is the empty set. Any partition can be seen as a classification map, where each subset Ω_i characterizes a class, that is

$$\Omega_i = \{z \in \Omega / z \text{ belongs to the i}^{\text{th}} \text{ class}\}. \tag{43}$$

The boundary of a subset Ω_i is defined as

$$\begin{aligned} \Gamma_i &= \partial\Omega_i \cap \Omega \\ &= \bigcup_{j\neq i} \Gamma_{ij} \end{aligned} \tag{44}$$

where

$$\Gamma_{ij} = \Gamma_{ji} = \Gamma_i \cap \Gamma_j \cap \Omega \tag{45}$$

is the interface between two regions and can eventually be equal to $\emptyset$.

Giving the definitions mentioned earlier, the classification of a data function $I : \Omega \rightarrow \mathbb{R}$ over Ω with respect to K predefined classes consists in finding the optimum set $\{\Omega_i\}_{i=1\ldots K}$ constrained to the following conditions.

1) The set $\{\Omega_i\}_{i=1\ldots K}$ representing the final classification map is a partition of Ω, i.e., the conditions in (42) are fulfilled.
2) The data of a given class are well described by the class first- and second-order statistics, i.e., the smaller the standard deviation, the closer the elements are to the mean value.
3) The solution is regular, i.e., small isolated regions are avoided.

The proposed solution considers the evolution of coupled active interfaces until the optimum partition is reached. The evolution itself is guided by functionals or forces, derived from the constraints mentioned earlier. It is performed considering a multiphase level-set scheme [85], i.e., each region and its corresponding interface are described by a level-set function $\Theta_i(x, y; t)$ such that

$$\begin{cases} \Theta_i(x, y; t) > 0 & \text{if } (x, y) \in \Omega_i \\ \Theta_i(x, y; t) = 0 & \text{if } (x, y) \in \Gamma_i \\ \Theta_i(x, y; t) < 0 & \text{otherwise} \end{cases} \tag{46}$$

where x and y represent the spatial coordinates and t indicates the variation of the level-set function with time. According to (46), the front, i.e., the interface of a certain region, is composed of points where the level-set function equals zero, whereas the interior of a certain region is marked by the positive values of the level set. While the tracking of drastic topological changes, such as boundary breaking and merging, is very difficult when evolving directly the curves, it is automatic when using the level-set representation, justifying its use. Furthermore, all required calculations are performed on a fixed rectangular grid, allowing for accurate numerical approximations of the level-set motion [77], [85].

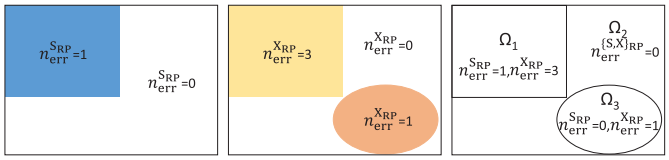

Fig. 18. Pictorial representation of (Left) S-band phase partially corrupted by a one-cycle unwrapping error, (Middle) X-band phase partially corrupted by a three-cycle unwrapping error in the top-left corner and one-cycle unwrapping error in the bottom-right corner, and (Right) optimum partition.

B. Active Contours for DFDB Unwrapping Error Correction

In the context of our DFDB unwrapping error correction, the observed data are the available residual phases, i.e., $\phi_{\text{res}}^{\text{X}_{\text{RP}}}$, $\phi_{\text{res}}^{\text{S}_{\text{RP}}}$, $\phi_{\text{res}}^{\text{X}_{\text{SP}}}$, and $\phi_{\text{res}}^{\text{S}_{\text{SP}}}$. Rather than segmenting the phase itself, the goal here is to detect and classify only regions representing 2π ambiguities. Hence, the classification is performed over the following data difference functions:

$$\begin{aligned} u_{\text{X}} &= \phi_{\text{res}}^{\text{X}_{\text{RP}}} - k_{z,\text{real}}^{\text{X}_{\text{RP}}} h_{\text{ref,SP}}, \quad u_{\text{X}} : \Omega \rightarrow \mathbb{R} \\ u_{\text{S}} &= \phi_{\text{res}}^{\text{S}_{\text{RP}}} - k_{z,\text{real}}^{\text{S}_{\text{RP}}} h_{\text{ref,SP}}, \quad u_{\text{S}} : \Omega \rightarrow \mathbb{R} \\ u_{\text{SX}} &= \phi_{\text{res}}^{\text{S}_{\text{RP}}} - \frac{k_{z,\text{real}}^{\text{S}_{\text{RP}}}}{k_{z,\text{real}}^{\text{X}_{\text{RP}}}} \phi_{\text{res}}^{\text{X}_{\text{RP}}}, \quad u_{\text{SX}} : \Omega \rightarrow \mathbb{R} \end{aligned} \tag{47}$$

where $h_{\text{ref,SP}}$ is obtained from the weighted average of the single-pass residual heights, which, as mentioned earlier, are considered free of unwrapping errors.

The ith region—or, equivalently, the ith class—characterizes the unwrapping errors in both the X- and S-band data, i.e., it is described by

$$\Omega_i = \left\{ p \in \Omega \,\middle|\, \begin{matrix} n_{\text{err}}^{\text{X}_{\text{RP}}}[p] = n_{\text{err}}^{\text{X}_{\text{RP}}}{}_i \\ n_{\text{err}}^{\text{S}_{\text{RP}}}[p] = n_{\text{err}}^{\text{S}_{\text{RP}}}{}_i \end{matrix} \right\} \tag{48}$$

where the integers $n_{\text{err}}^{\text{X}_{\text{RP}}}{}_i$ and $n_{\text{err}}^{\text{S}_{\text{RP}}}{}_i$ represent the X- and S-band repeat-pass ambiguity errors of the class. Therefore, the final classification provides an ambiguity map with all the necessary information for correcting the interferometric data. A pictorial representation of two corrupted X- and S-band phases and the corresponding partition can be seen in Fig. 18

The approach proposed here intends to cope with two main issues related to the use of the single-/repeat-pass configuration: the presence of biases in the repeat-pass phases or in the reference phases and the false detection of unwrapping errors due to noise scaling. Accordingly, the classification constraints are defined as follows.

1) The set $\{\Omega_i\}_{i=1\ldots K}$ representing the final classification map is a partition of Ω.
2) Within a region, the X-band data approach in average the ambiguity band of the corresponding class up to a small bias.
3) Within a region, the S-band data approach in average the ambiguity band of the corresponding class up to a small bias.
4) The difference between the X- and S-band residual height maps is minimal.
5) The detected discontinuities in the phase differences correspond to discontinuities in the individual phases.

6) The solution is regular, i.e., small isolated regions are avoided.

The above-mentioned constraints are analytically described by the following functionals.

1) *Partition Functional:*

$$F_1(\Theta_1,\ldots,\Theta_K)=\int_\Omega\left(\sum_{i=1}^{K}H(\Theta_i)-1\right)^2 dxdy. \quad (49)$$

2) *X-band Data Matching Functional:*

$$F_2(\Theta_1,\ldots,\Theta_K)=\sum_{i=1}^{K}\int_{\Omega_i}\left(\frac{u_{\mathrm{X}}-2\pi n_{\mathrm{err}\,i}^{\mathrm{X_{RP}}}}{\sigma_{\mathrm{X}}}\right)^2 H(\Theta_i)dxdy \quad (50)$$

where σ_{X} is the differential phase standard deviation given by

$$\sigma_{\mathrm{X}}=\sqrt{\sigma_{\mathrm{X_{RP}}}^2+k_{z,\mathrm{real}}^{\mathrm{X_{RP}}}\sigma_{\mathrm{ref}}^2} \quad (51)$$

and $\sigma_{\mathrm{X_{RP}}}$ is estimated from the repeat-pass interferometric coherence. This functional penalizes differences between the topographic information obtained from the single-pass reference and the X-band repeat elevation model after the unwrapping error correction. However, it is weaker whenever u_{X} is deemed unreliable, i.e., when the noise level in the X-band repeat-pass phase and/or reference residual height model is high.

3) *S-band Data Matching Functional:*

$$F_3(\Theta_1,\ldots,\Theta_K)=\sum_{i=1}^{K}\int_{\Omega_i}\left(\frac{u_{\mathrm{S}}-2\pi n_{\mathrm{err}\,i}^{\mathrm{S_{RP}}}}{\sigma_{\mathrm{S}}}\right)^2 H(\Theta_i)dxdy \quad (52)$$

where σ_{S} is the differential phase standard deviation given by

$$\sigma_{\mathrm{S}}=\sqrt{\sigma_{\mathrm{S_{RP}}}^2+k_{z,\mathrm{real}}^{\mathrm{S_{RP}}}\sigma_{\mathrm{ref}}^2} \quad (53)$$

and $\sigma_{\mathrm{S_{RP}}}$ is estimated from the repeat-pass interferometric coherence. Note that (51) and (53) assume the statistical independence of single- and repeat-pass data sets, which is not strictly the case since the two interferometric phases share the same master. However, due to the large difference between the single- and repeat-pass baselines, the dependence between the two data sets can be neglected [86].

4) *Dual-Frequency Data Matching Functional:*

$$F_4(\Theta_1,\ldots,\Theta_K)=\sum_{i=1}^{K}\int_{\Omega_i}\left(\frac{u_{\mathrm{S}}-2\pi n_{\mathrm{err}\,i}^{\mathrm{S_{RP}}}-\left(u_{\mathrm{X}}-2\pi n_{\mathrm{err}\,i}^{\mathrm{X_{RP}}}\right)\cdot\frac{k_{z,\mathrm{real}}^{\mathrm{S_{RP}}}}{k_{z,\mathrm{real}}^{\mathrm{X_{RP}}}}}{\sigma_{\mathrm{SX}}}\right)^2 H(\Theta_i)dxdy. \quad (54)$$

This data functional penalizes the differences between the topographic information obtained from both repeat-pass data sets after the unwrapping error correction. The smaller the variance of u_{XS} is, the stronger is the penalization.

5) *Edge-Detection Functional:*

$$F_5(\Theta_1,\ldots,\Theta_K)=\sum_{i=1}^{K}\int_\Omega g\left(\phi_{\mathrm{res}}^{\mathrm{X_{RP}}},\phi_{\mathrm{res}}^{\mathrm{S_{RP}}}\right)\delta(\Theta_i)|\nabla\Theta_i|dxdy \quad (55)$$

where $g(\cdot)$ assumes zero on edges and a positive value otherwise.

The functional penalizes the introduction of new edges in the individual phases, regularizing the result and avoiding the false alarm due to biases in the repeat-pass data.

6) *Regularization Functional:*

$$F_6(\Theta_1,\ldots,\Theta_K)=\sum_{i=1}^{K}\int_\Omega\delta(\Theta_i)|\nabla\Theta_i|dxdy. \quad (56)$$

The final global functional is given by the weighted summation

$$F(\Theta_1,\ldots,\Theta_K)=\sum_{l=1}^{6}\xi_l F_l(\Theta_1,\ldots,\Theta_K) \quad (57)$$

where $\xi_{1\ldots6}$ are predefined weights. Since the three data functionals are weighted by the appropriate standard deviations, it is enough to consider a single weight for the data terms, i.e., $\xi_2=\xi_3=\xi_4$.

The minimization is performed by solving the system of coupled partial differential equations (PDEs) given by

$$\frac{\partial F_\varepsilon}{\partial\Theta_i}=0,\quad \forall i=1\ldots K,\ \varepsilon\to0^+ \quad (58)$$

where F_ε is the regular approximation of (57) [76] (see the Appendix for the solution).

The strength of the approach lies on the natural evolution of the detected regions toward the minimum DFDB differences. Since the classification is applied on the phase differences, natural boundaries in the scene due to changes in topography are preserved. Moreover, thanks to the dual-frequency data functional, biases large enough to cause errors in the initial X-band classification map, but not in the S-band one, do not disrupt the final results. Additionally, the edge-detection functional avoids the placement of false discontinuities. Finally, the introduction of salt-and-pepperlike errors is mitigated through the use of the regularization functional.

C. Validation With Simulated and Real Data

In the following, simple simulations are used to highlight the importance of the introduced functionals and the effectiveness of the proposed strategy. For simplicity, the elevation model to be retrieved is zero everywhere, and the single-pass phases are always assumed free of artifacts. All images contain 128 × 128 pixels. A square-shaped unwrapping error is introduced in both repeat-pass phases, with $n_{\mathrm{err}}^{\mathrm{S_{RP}}}=1$ and $n_{\mathrm{err}}^{\mathrm{X_{RP}}}=3$. This represents a challenging case for the DFDB configuration, since both the phases are affected at the same location, and

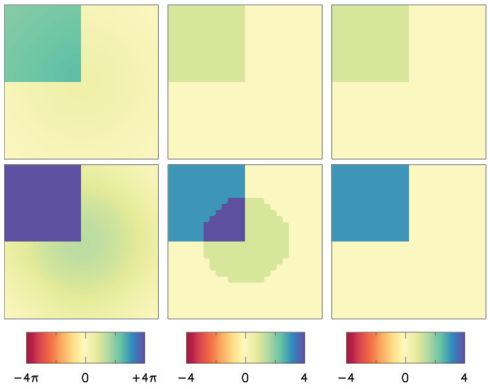

Fig. 19. In this simulated scenario, no noise is included, and the only phase content of the repeat-pass data are square-shaped unwrapping errors with $n_{\text{err}}^{\text{S}_{\text{RP}}} = 1$ and $n_{\text{err}}^{\text{X}_{\text{RP}}} = 3$ (in the top-left quadrant of the images) and a low-pass artifact emulating uncompensated azimuth-varying range delays. (Top row) S-band data. (Bottom row) X-band data. (From left to right) Corrupted repeat-pass phases, unwrapping error maps obtained using no dual-frequency data functional during the evolution, and unwrapping error maps obtained using the dual-frequency data functional.

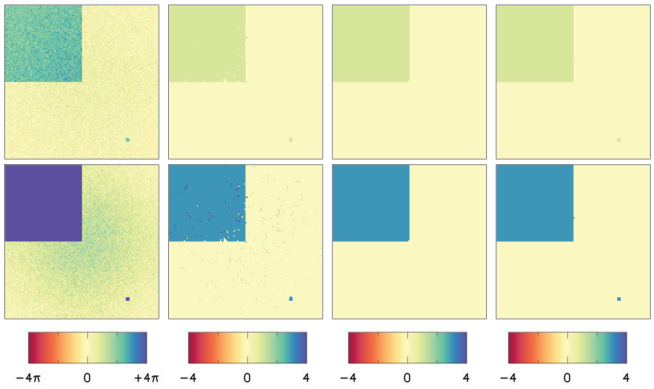

Fig. 20. In this simulated scenario, Gaussian noise with a standard deviation of 50° is included in the repeat-pass phases. The first column shows the (Top) S-band repeat-pass phase and (Bottom) X-band repeat-pass phase. In addition to the unwrapping error of the first simulation, a small error in the bottom-right quadrant is introduced. The results of three trials are depicted in the second–fourth columns: the first one considers no smoothing functional, i.e., $\xi_5 = \xi_6 = 0$, the second one considers only the traditional regularization functional, i.e., $\xi_5 = 0$ and $\xi_6 = 1$, and the third considers additionally the edge-detection regularization $\xi_5 = \xi_6 = 1$.

$n_{\text{XRP}}/n_{\text{SRP}} \approx \lambda_{\text{S}}/\lambda_{\text{X}}$, i.e., the initial dual-frequency phase difference is close to zero.

The first simulation intends to show the strength of the dual-frequency data functional. For that, no noise is included and regularization and edge-detection functionals are set to zero. The repeat-pass X-band phase is corrupted by a low-pass error varying from 0° to 250°. The same pattern is scaled by the ratio between the X- and S-band wavelengths and applied to the S-band repeat-pass phase, thus emulating the effect of uncompensated azimuth-varying range delays in dual-frequency simultaneous acquisitions. The corrupted phases can be seen in the first column of Fig. 19 (S-band at the top and X-band at the bottom). The first trial considers $\xi_4 = 0$, i.e., no dual-frequency functional. The unwrapping error maps obtained with the multiphase evolution are shown in the second column of Fig. 19, where the top corresponds to S-band and the bottom corresponds to X-band. In this case, large unwrapping errors were introduced in the X-band phase due to the bias. When considering $\xi_4 = 1$, the case presented in the third column of Fig. 19, the evolution converges to the desired partition.

For the second example, the simulated phases include Gaussian noise with the standard deviations of 50° for the repeat-pass phases and 250° for the scaled single-pass reference. The same low-pass artifact of the first experiment is considered. An additional unwrapping error (4×4 pixels) is introduced in the bottom-right quadrant, as can be seen in the first column of Fig. 20 (S-band at the top and X-band at the bottom). In this example, all data functionals are used, and the goal is to demonstrate the capability of the edge-detection functional to avoid the introduction of errors due to noise scaling. For that purpose, the results of three trials are presented: the first one considers no smoothing functional, i.e., $\xi_5 = \xi_6 = 0$, the second one considers only the traditional regularization functional, i.e., $\xi_5 = 0$ and $\xi_6 = 1$, and the third considers additionally the edge-detection regularization $\xi_5 = \xi_6 = 1$. The retrieved unwrapping error maps are presented in the second–fourth columns of Fig. 20. As expected, if no regularization is employed, the obtained correction is noisy. The results are improved by using the curve length regularization functional. However, the small unwrapping error introduced in this example is completely missed. Considering the edge-detection functional, it is possible to obtain a compromise between a regular solution and the detection of small unwrapping errors.

As it is, the approach is able to successfully map unwrapping errors in noisy cases and in the presence of small biases. However, if errors large enough to cause misdetection simultaneously in repeat- and single-pass phases are present, the estimation can fail. Moreover, even if the errors are not large enough to compromise the retrieved map, the rough estimation and removal of low-pass errors can improve the convergence of the multiphase evolution. Therefore, the following bias estimation is proposed at this stage:

$$\phi_{\text{off,S}} = \frac{\sum_{n=1}^{N} \langle u_{\text{S}} \rangle_{2\pi}}{N} \tag{59}$$

where $\langle \cdot \rangle_{2\pi}$ represents the *modulo* 2π operator, and the average is performed over a (preferably large) window containing N pixels. The offset is computed prior to the classification and is used to update the data functions in (47) and initial classification map in (40). Note that the estimation is performed over the data set with a larger HoA, in this case, the S-band. In fact, the estimation is limited to errors up to a wrapping cycle of this data set. Note that this step only represents a coarse bias estimation, and it will not be used to correct the repeat-pass phases at this point of the processing chain. A finer strategy to remove low-pass components in the DFDB configuration is discussed in Section VIII.

Finally, a block of real F-SAR DFDB data is considered. Fig. 21 shows the S-band unwrapped phase after

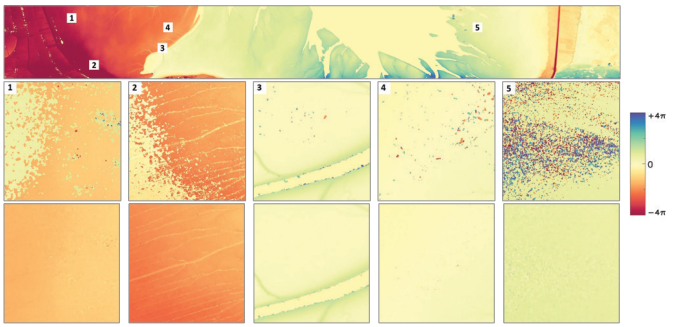

Fig. 21. (Top) Unwrapped S-band phase after calibration. (Middle) Phase of the ROIs 1–5 are shown from left to right after correcting unwrapping errors by simply using the single-pass phases as reference. (Bottom) Results obtained with the active-contour-based approach using no external weighting of the functionals (i.e. $\xi_{1\ldots6} = 1$).

calibration, and a large unwrapping error is recognized by the color transition from orange to yellow, from left to right. The error is related to a low coherent water branch, which divides the image in two regions and cripples the growing process. Despite the apparent simplicity of the detection, the direct estimation of residual ambiguities using the single-pass information only [i.e., using (40)] is impaired by the presence of noise and low-pass phase artifacts. In this case, the remaining (and introduced) artifacts can be observed in the regions of interest (ROIs) in the second row of Fig. 21, which shows the phases after the correction using (40). On the other hand, the active-contour scheme proposed in this section is able to provide satisfactory results, as seen in third row of Fig. 21. Moreover, the comparison of the final obtained F-SAR DEMs and the ALS reference in Section X shows no remaining large-scale unwrapping errors around the water branch (see Figs. 30 and 32).

VIII. Estimation of Low-Pass Artifacts in the Repeat-Pass Data

Repeat-pass interferometry is generally more sensitive to low-frequency distortions in comparison with single-pass interferometry due to the separate acquisition of master and slave data sets. The causes, and consequently, the characteristics of such artifacts depend on several factors, e.g., the type of platform employed, the precise knowledge of the system parameters, and the processing kernel, among others. Assuming that no deformation takes place in the time between master and slave acquisitions and that soil moisture remains the same, the main sources of low-frequency disturbances in airborne InSAR are baseline miscalibration, propagation effects in the troposphere, and uncompensated residual motion errors.

After phase-to-height conversion, repeat-pass and single-pass residual height maps can be modeled as

$$h_{\mathrm{res},\{\mathrm{X,S}\}_{\mathrm{RP}}} = h_{\mathrm{top}} + h_{\varepsilon,\{\mathrm{X,S}\}_{\mathrm{RP}}} + h_{\eta,\{\mathrm{X,S}\}_{\mathrm{RP}}} \tag{60}$$

and

$$h_{\mathrm{res},\{\mathrm{X,S}\}_{\mathrm{SP}}} = h_{\mathrm{top}} + h_{\eta,\{\mathrm{X,S}\}_{\mathrm{SP}}} \tag{61}$$

where h_{top} is the desired topographic information, $h_{\eta,*}$ are the noise contributions, and $h_{\varepsilon,*_{\mathrm{RP}}}$ represent the low-frequency disturbances. It is considered here that any other phase artifact can be neglected for the single-pass case, which is typically true if a proper calibration of the phase offset and multipath component has been previously carried out. Moreover, the topographic component in the X- and S-band data is assumed to be the same, i.e., penetration depth differences are neglected.

In order to mitigate the effects of low-frequency artifacts in the final elevation model, the information of single- and repeat-pass data is combined. For the proposed strategy, the spectrum of $h_{\varepsilon,*}$ is considered to be limited and an additive noise model is employed, where all the $h_{\eta,*}$ values are assumed to be zero-mean and pairwise independent. Moreover, $h_{\varepsilon,*}$ is assumed to be stationary and independent of the noise contributions. The hypothesis of stationarity requires the approach to be applied in a blockwise manner, with a block size chosen according to the spatial variation observed in the residual height differences.

Considering that all retrieved elevation models have the same resolution cell and are coregistered to the same geometry, the final X-band and S-band residual height can be estimated as

$$h_{\mathrm{res},\{\mathrm{X,S}\}} = h_{\mathrm{res},\{\mathrm{X,S}\}_{\mathrm{RP}}} - (h_{\mathrm{res},\{\mathrm{X,S}\}_{\mathrm{RP}}} - h_{\mathrm{res},\{\mathrm{X,S}\}_{\mathrm{SP}}}) \circledast g_{\mathrm{op}} \tag{62}$$

where g_{op} is the optimum low-pass filter, the symbol $\circledast$ represents the convolution, and range and azimuth dependences are suppressed for simplicity.

Treating separately X- and S-band data sets requires no assumptions regarding the same topographic content. On the other hand, by performing a joint estimation of the residual error, one can benefit from the fact that errors originating from uncompensated residual motion errors or propagation in the troposphere are mainly the same in both residual height maps due to the simultaneous acquisition. This information can then be used for the construction of g_{op}. Specifically, we assume that $h_{\varepsilon,X_{\mathrm{RP}}} = h_{\varepsilon,S_{\mathrm{RP}}} = h_{\varepsilon}$ and that the error can be estimated from the residual height map with higher relative accuracy (in our case, the X-band one) using a narrowband low-pass filter, e.g., a fifth-order Butterworth filter [87], that is

$$\hat{h}_{\varepsilon} = (h_{\mathrm{res,X_{RP}}} - h_{\mathrm{ref,SP}}) \circledast g_{\mathrm{op}} \tag{63}$$

with cutoff wavelength w_c obtained as the solution of

$$\min_{w_c} R_{\mathrm{dual}} \triangleq \min_{w_c} \sum |h_{\mathrm{diff,X}} - h_{\mathrm{diff,S}} \circledast g_{\mathrm{op}}(w_c)|^2 \tag{64}$$

where

$$h_{\mathrm{diff},\{\mathrm{X,S}\}} = h_{\mathrm{res},\{\mathrm{X,S}\}_{\mathrm{RP}}} - h_{\mathrm{res},\{\mathrm{X,S}\}_{\mathrm{SP}}}. \tag{65}$$

For large cutoff wavelengths, the out-of-band noise in the S-band height difference tends to increase the dual-frequency residual R_{dual}. On the other hand, if w_c is too short, part of the information of the disturbance itself is missed, also leading to increased R_{dual}. By solving (64), a compromise can be found. The corrected residual elevation maps are then retrieved by simply subtracting the estimated errors, that is

$$h_{\mathrm{res},\{\mathrm{X,S}\}} = h_{\mathrm{res},\{\mathrm{X,S}\}_{\mathrm{RP}}} - \hat{h}_{\varepsilon}. \tag{66}$$

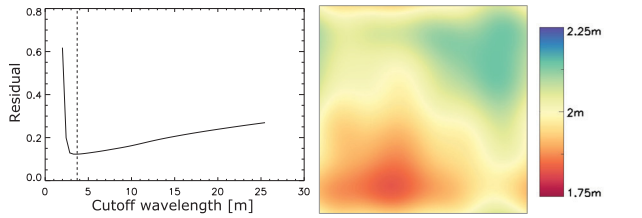

Fig. 22. (Left) Variation of the dual-frequency residual difference for different cutoff wavelengths for a block of real DFDB F-SAR data of around 500 m × 500 m. (Right) Estimated low-pass disturbance using the obtained optimum cutoff wavelength.

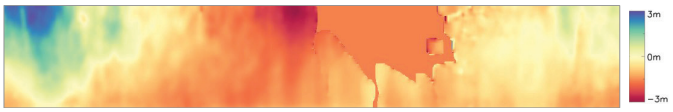

Fig. 23. Estimated height error in the X- and S-band elevation models due to low-frequency disturbances.

A limitation of the low-pass estimation is the inclusion of the in-band noise of the single-pass reference height $h_{\mathrm{ref,SP}}$ in the estimated disturbance. The effect is more relevant the stronger the noise, and the wider the bandwidth of the low-frequency disturbances.

Fig. 22 (left) shows an example of the variation of R_{dual} for different values of w_c for a block of around 500 m × 500 m extracted from the F-SAR DFDB campaign over the Jade Bight. In this case, the minimum residual difference corresponds to a cutoff wavelength of around 4 m. In Fig. 22 (right), the low-pass disturbance estimated for the block using the optimum cutoff frequency is shown. Finally, Fig. 23 shows the estimated height error for the whole imaged scene.

IX. Estimation of the Underlying Topography

After the removal of the spatially correlated disturbances, the elevation models in slant-range geometry corresponding to each frequency of acquisition can be estimated as

$$\hat{h}_{\mathrm{X,S}} = h_{\mathrm{res},\{\mathrm{X,S}\}} \cdot U + h_{\mathrm{res},\{\mathrm{X,S}\}_{\mathrm{SP}}} \cdot (1-U) + h_{\mathrm{ref}} \quad (67)$$

where $h_{\mathrm{res},\{\mathrm{X,S}\}}$ are the results of (66), h_{ref} is the reference DEM used to support the SLC focusing and interferometric processing, and U is a binary mask assuming 0 if the unwrapping of repeat-pass data is failed, indicating strongly decorrelated areas (e.g., volume scatterers). Considering that master and slave acquisitions are obtained within a short time span, the expected height standard deviations of the repeat-pass models for surface scatterers are typically much smaller than those of the single-pass models. Hence, in order to avoid the introduction of residual multipath artifacts in the final elevation map and to avoid its degradation due to the under estimation of the noise levels in the single-pass data, we use the formulation in (67). If, on the other hand, volume decorrelation plays a role, e.g., for agricultural fields with tall crops, a weighted average (or a true ML solution) should be considered instead.

Depending on the characteristics of the imaged scene and the required absolute vertical accuracy, the differences in the X- and S-band wave penetration can be considered negligible, e.g., when imaging bare land. In this case, X- and S-band DEMs can be merged into a higher quality DFDB elevation model. For that, we propose here a simple fusion scheme in the wavelet domain.

A. Multiresolution Analysis for Height Extraction

The decorrelation and compressing properties of wavelet transforms offer a powerful tool for data denoising. Accordingly, the topic has been widely investigated by the image processing community [88]–[92] and by the SAR community for SLC despeckling [93]–[95], interferometric phase denoising [96]–[98], and mitigation of atmospheric noise [99], [100]. In general, wavelet domain filters benefit from the fact that the wavelet transform maps most of the signal energy into a few large coefficients. Rather than filtering out high-frequency components, i.e., smoothing the data, the denoising algorithms try to identify and remove wavelet coefficients that represent pure noise. Moreover, wavelet transforms allow for a multiresolution characterization of the data, favoring the proper handling of nonstationary signal and noise [101]–[103].

The fusion scheme proposed in the following is based upon the techniques in [99] and [100], and its main motivations are: 1) multiresolution wavelet analysis potentially allows for the estimation of the actual statistics of the individual elevation models and 2) the redundancy of the multichannel configuration combined with the decorrelation capabilities of discrete wavelet transforms can be exploited to provide additional noise and artifact reduction in an efficient manner.

The inputs for our estimation are the X- and S-band elevation models obtained through (67), that is

$$h_{\mathrm{X,S}} = h_{\mathrm{top}} + h_{\eta,\{\mathrm{X,S}\}} \quad (68)$$

where h_{top} is the desired topographic component and $h_{\eta,\{\mathrm{X,S}\}}$ is the noise with spatially varying standard deviation. Considering the linearity of the wavelet transform, the additive model in (68) is transferred to the wavelet domain, that is

$$\mathbf{W}_{\mathrm{X,S}} \triangleq W(h_{\mathrm{X}}) = \mathbf{W}_{h_{\mathrm{top}}} + \mathbf{W}_{h_{\eta,\{\mathrm{X,S}\}}} \quad (69)$$

where $W(\cdot)$ is the wavelet operator. Moreover, considering that noise and topography components are independent and an orthogonal wavelet basis is considered, the noise in the wavelet domain at a certain level can also be characterized as zero-mean Gaussian with spatially varying standard deviation $\sigma_{\eta,\{\mathrm{X,S}\}}$ [104].

In practice, we make use of the discrete wavelet transform performing a multiresolution decomposition of the images, where each level (or scale) is obtained by successively filtering and downsampling the input image leading to four subbands: one corresponding to the low-frequency or *smooth* band denoted by W_{LL_j} (low–low) and three detail bands denoted by W_{HL_j}, W_{LH_j}, W_{HH_j} (high–low, low–high, and high–high, respectively).

The smooth bands are further decomposed until the coarsest (or highest) scale has been achieved, yielding one residual low-passband ($W_{\{\mathrm{X,S}\}_{\mathrm{LL}_J}}$) and $3J$ detail bands for each frequency of acquisition, where J is the desired number of scales.

Provided that the noise is not dominant, i.e., considering that its standard deviation is considerably smaller than the expected topography, its wavelet coefficients have small magnitude and are distributed over all scales. On the other hand, the discrete wavelet transform of the terrain is sparse, i.e., the energy is concentrated in a limited number of coefficients. In fact, as suggested in [99], most of the topography can be modeled as a $1/f$ process, i.e., most of the signal energy follows a polynomial decay when transitioning from coarser to finer scales. In this sense, the wavelet transform properly decorrelates h_{top} and can be understood as the approximation of its Karhunen–Loeve transform [99], [105]. Since the lower (or finer) scales contain mainly noise, they can be used for assessing the statistics of the individual height maps [104]–[106]. The final elevation model can then be estimated by properly identifying and merging the relatively few signal coefficients while attenuating or suppressing the coefficients which characterize only noise, thus obtaining a smoother solution.

Although most of the energy of h_{top} is compressed into large magnitude coefficients at higher (or coarser) scales, the wavelet coefficients of fine features, e.g., edges of building or small terrain fissures, can be spread throughout the lower scales, eventually assuming small magnitudes. Consequently, if not performed carefully, the suppression of coefficients in the lower scales can lead to oversmoothing or even to the suppression of terrain traits.

B. DFDB Multiresolution Analysis for Height Extraction

In order to distinguish between features and noise, the redundancy of the multichannel configuration can be exploited. Specifically, the cross correlation between the multiresolution decompositions of X- and S-band elevation models is evaluated. Intuitively, whenever the detail bands contain terrain features, a high correlation between the X- and S-band coefficients is expected. On the other hand, assuming the independence of the noise contributions of both data sets, low correlation is expected for the noise coefficients.

The proposed fusion scheme can be described by the following steps.

1) Compute the multiresolution decomposition of X- and S-band elevation models up to the J scale. Considering that the main goal is to reduce the impact of noise, it is enough to set J to a small number, e.g., $J = 3$, as suggested for the interferometric phase filtering in [96]. Alternatively, the scales dominated by noise can be identified by evaluating the mean power of each decomposition level of the difference between X- and S-band height maps, i.e., W_{XS}, since the height difference should contain mainly noise at this stage.
2) For Each Decomposition Level j:
   a) Estimate the cross correlation between the detail bands of X- and S-band decompositions, i.e., compute

$$R_{W_{\{\text{LH,HL,HH}\}_j}}[i_n, i_m] = \text{corr}(W_{\text{X}_{\{\text{LH,HL,HH}\}_j}}, W_{\text{S}_{\{\text{LH,HL,HH}\}_j}}). \quad (70)$$

   Considering that the noise contributions are zero-mean, independent, and that their statistics are homogeneous in the considered estimation window, then $R_{W_{*_j}} \to 0$ when no signal is present. On the other hand, if the coefficients represent the desired signal, then $R_{W_{*_j}} \to 1$.
   b) Locally estimate the expected noise statistics as

$$\hat{\sigma}_{\eta_j,\{\text{X,S}\}}[i_n, i_m] = \frac{1}{M_j} \sum_{i_n \in \delta_N} \sum_{i_m \in \delta_N} |W_{\{\text{X,S}\}_{\text{HH}_j}}[i_n, i_m]|^2 \quad (71)$$

   where δ_N is the estimation window used to account for the spatial variability of the noise and M_j is the number of available pixels [103].
   c) Estimate the detail coefficients as

$$\hat{W}_{\text{LH}_j} = \frac{\left(W_{\text{X}_{\text{LH}_j}}/\hat{\sigma}^2_{\eta_j,\text{X}} + W_{\text{S}_{\text{LH}_j}}/\hat{\sigma}^2_{\eta_j,\text{S}}\right)}{\left(1/\hat{\sigma}^2_{\eta_j,\text{X}} + 1/\hat{\sigma}^2_{\eta_j,\text{S}}\right)} R_{W_{\text{LH}_j}} \quad (72)$$

$$\hat{W}_{\text{HL}_j} = \frac{\left(W_{\text{X}_{\text{HL}_j}}/\hat{\sigma}^2_{\eta_j,\text{X}} + W_{\text{S}_{\text{HL}_j}}/\hat{\sigma}^2_{\eta_j,\text{S}}\right)}{\left(1/\hat{\sigma}^2_{\eta_j,\text{X}} + 1/\hat{\sigma}^2_{\eta_j,\text{S}}\right)} R_{W_{\text{HL}_j}} \quad (73)$$

   and

$$\hat{W}_{\text{HH}_j} = \frac{\left(W_{\text{X}_{\text{HH}_j}}/\hat{\sigma}^2_{\eta_j,\text{X}} + W_{\text{S}_{\text{HH}_j}}/\hat{\sigma}^2_{\eta_j,\text{S}}\right)}{\left(1/\hat{\sigma}^2_{\eta_j,\text{X}} + 1/\hat{\sigma}^2_{\eta_j,\text{S}}\right)} R_{W_{\text{HH}_j}}. \quad (74)$$

3) At scale J, estimate the low-pass residual as

$$\hat{W}_{\text{LL}_J} = \frac{\left(W_{\text{X}_{\text{LL}_J}} + W_{\text{S}_{\text{LL}_J}}\right)}{2}. \quad (75)$$

4) Compute the inverse decomposition from the estimated wavelet coefficients in (72)–(75).

If required, the above-described approach can be modified to better accommodate differences in the X- and the S-band topography. In this case, instead of estimating a single set of wavelet coefficients that are then inverted to provide the final elevation model, the wavelet decompositions of X- and S-band data are individually estimated. Specifically, (72)–(74) are replaced by

$$\hat{W}_{\{\text{X,S}\}_{\text{LH,HL,HH}_j}} = W_{\{\text{X,S}\}_{\text{LH,HL,HH}_j}} R_{W_{\{\text{X,S}\}_{\text{LH,HL,HH}_j}}} \quad (76)$$

i.e., the coefficients that are more likely to represent only noise are suppressed. Notice that the correlation coefficients in (76) are now modified in order to avoid the smearing of features present in only one of the individual data sets. For that purpose, a further assumption is required, namely that the detail coefficients of features have larger magnitudes than the ones of noise. In this case,

$$R_{W_{\{\text{X,S}\}_{\{\text{LH,HL,HH}\}_j}}} = \begin{cases} R_{W_{\{\text{LH,HL,HH}\}_j}}, & W_{\{\text{X,S}\}_{\{\text{LH,HL,HH}\}_j}} < \zeta_{\{\text{LH,HL,HH}\}_j} \\ 1, & W_{\{\text{X,S}\}_{\{\text{LH,HL,HH}\}_j}} > \zeta_{\{\text{LH,HL,HH}\}_j} \end{cases} \quad (77)$$

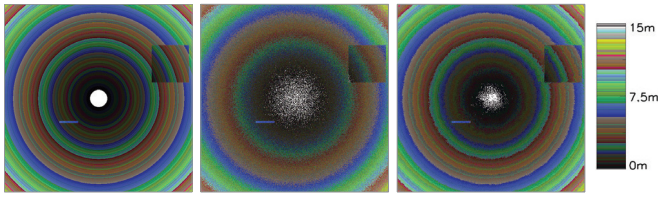

Fig. 24. (Left) Simulated terrain containing abrupt variations. (Middle) Result of ML estimation. (Right) Result of wavelet fusion using four decomposition levels. A qualitative color palette was chosen for the depiction of simulated and real terrains, since such palette favors a better visualization of noise and its reduction.

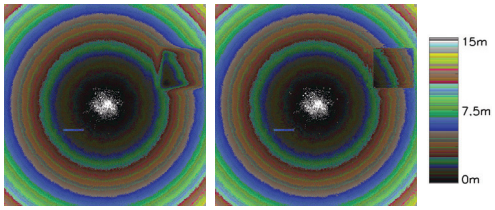

Fig. 25. In this experiment, the true topography differs in S- and X-band data sets. (Left) X-band wavelet-based estimation without considering the modification of the correlation coefficients. (Right) Result considering the modification.

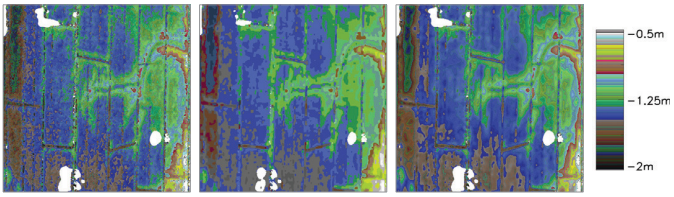

Fig. 26. Validation of the wavelet domain estimation using real data. (From left to right) ML estimation, MAP+TV estimation, and wavelet-based estimation. Both wavelet and MAP+TV estimations provide good noise reduction in comparison with the ML estimation.

Fig. 27. Optical image of the Jade Bight, northern Germany. The red rectangle indicates the valid area imaged by the F-SAR and corresponds to a total size of approximately 20 km × 3 km.

where ζ_{*_j} are thresholds calculated from the data using the maximum absolute deviation of the subbands [88]. Note that, while the modification of the correlation coefficients mitigates the smearing of features, it can also lead to suboptimal performance for very noisy data sets.

C. Validation With Simulated and Real Data

Results considering a simulated terrain embedded in noise are shown in Fig. 24. The original elevation model, the result of a simple ML estimator [13], and the result of the proposed approach appear from left to right, respectively. For the wavelet fusion, Daubechies wavelets and four decomposition levels were considered [107]. Moreover, for this first simulation, it was assumed that the topographic content of X- and S-band data are the same. It is possible to see that the wavelet fusion provides good results in terms of noise reduction and preservation of features. Moreover, the overall computation cost is low thanks to the efficiency of the discrete wavelet transform [106].

The results in Fig. 25 validate the use of the modified coefficients in (76). For this simulation, the rectangular feature in the top-right quadrant appears only in the X-band data (emulating, e.g., short crops). Fig. 25 (left) shows the result of the individual X-band wavelet estimation without considering (77) (or equivalently, setting $\zeta_{*_j} = 0$). In Fig. 25 (right), the result, including the modified correlation coefficients, is given and shows a better preservation of the edges.

Finally, a block of real F-SAR DFDB data is considered. For comparison, in addition to the dual-frequency/wavelet-based and ML approaches, an MAP + total variation (MAP+TV) strategy is considered [108]. For both ML and MAP+TV estimations, we consider a modified likelihood function (F_{main}) profiting from the fact that the data have already been unwrapped

$$F_{\text{main}}(\boldsymbol{\Phi}|h) = \text{rect}\left(\frac{\phi_{\text{X}_{\text{RP}}}}{2\pi}\right) \prod_{i\in\{\text{S}_{\text{SP}},\text{S}_{\text{RP}},\text{X}_{\text{SP}},\text{X}_{\text{RP}}\}} f_i(\phi_i|h;\, L) \quad (78)$$

where $f_i(\phi_i|h;\, L)$ are the periodic likelihoods of the individual channels for a certain number of looks L, and the rectangular function (rect) limits the joint likelihood to one wrapping cycle of the fastest varying phase—here the X-band repeat-pass phase. Note that the low-frequency disturbances have to be compensated for in the interferometric phases, or, alternatively, the phases can be retrieved from the corrected residual height maps, that is

$$\phi_{\{\text{X,S}\}_{\text{RP}}} = h_{\text{res},\{\text{X,S}\}} k_{z,\text{real}}^{\{\text{X,S}\}_{\text{RP}}}. \quad (79)$$

The results are shown in Fig. 26, from left to right: ML, MAP+TV, and wavelet estimations. Both wavelet and MAP+TV estimations provide good noise reduction. The set of desired heights required for the MAP+TV approach was constrained around the X-band repeat-pass HoA (around 1.5 m) with a sampling of 0.001 cm. The total computational time required for the estimation of the 512 × 512 samples elevation map was less than 5 s for the wavelet approach and around 8 min for the MAP+TV approach. In both cases, the algorithms were implemented in interactive data language, with exception of the graph-cut optimizer required for the MAP+TV approach, implemented in C++.

X. Evaluation of Obtained Elevation Models

The data presented next were acquired on July 16, 2013, over the tidal flat areas of the Jade Bight, northern Germany, using the F-SAR system. An optical image of the scene is shown in Fig. 27.

TABLE II

PARAMETERS FROM F-SAR EXPERIMENT OVER THE JADE BIGHT, NORTHERN GERMANY

Parameter	X-band	S-band
Carrier Frequency [GHz]	9.784	3.25
Transmitted Bandwidth [MHz]	380	
Pulse Repetition Frequency (PRF) [Hz]	2232	
Azimuth Resolution [m]	0.5	
Range Resolution [m]	0.5	
Single-pass vertical baseline [m]	1.5	
Single-pass horizontal baseline [m]	0.4	
Repeat-pass vertical baseline [m]	20	
Repeat-pass horizontal baseline [m]	20	
Mean height above ground [m]	2420	

The campaign intended to generate a height map of the intertidal mud flats with a relative vertical precision of the order of centimeters on a grid with 1 m $\times$ 1 m sampling. Intertidal regions are extremely dynamic with severe changes in the water level during the course of the day. For such scenes, airborne sensors are more attractive in comparison with spaceborne sensors due to their flexibility in terms of acquisition time. Furthermore, the bight presents considerably lower backscatter than its surroundings. Thus, the quality of the acquired data is improved if the receiver gain can be controlled during the datatake, as it is the case of the F-SAR system. Moreover, the airborne system allows for the choice of the proper repeat-pass baseline, which enables the generation of DEMs fulfilling the accuracy requirements.

The experiment consisted of two passes during which the data were acquired simultaneously using the X- and S-band antennas. Additionally, the first flight was acquired with X- and S-band across-track interferometers. Thus, one master and two slaves were available for each carrier frequency, from which we computed one single-pass and one repeat-pass interferogram for each band, i.e., we construct a DFDB data set. The parameters of the experiment are summarized in Table II.

The multisquint algorithm was applied for the estimation of residual motion errors in the repeat-pass interferograms, and errors up to ± 3 cm in line of sight were removed, leading to an almost flat multisquint phase. No precise elevation model was used to support the image formation and the DEM generation chain. To account for topography during MoCo, spectral filtering, and flat-earth removal, a known mean elevation was considered. Note that since the terrain variation is relatively small for the majority of the scene (less than 15 m), the synthetic DEM constructed from the mean terrain height is enough to ensure a proper SLC focusing.

Within the valid swath, the HoA of the S-band repeat-pass data set varies from approximately 2 to 6 m, while the HoA of the X-band repeat-pass data set varies from approximately 0.7 to 2 m. On the other hand, single-pass interferograms have a much larger HoA ranging from around 100 to 200 m and 35 to 70 m for S- and X-band data, respectively. Hence, the unwrapping of the single-pass phases is straightforward considering the terrain variation of the scene. The residual interferometric phases obtained from the single-pass data sets

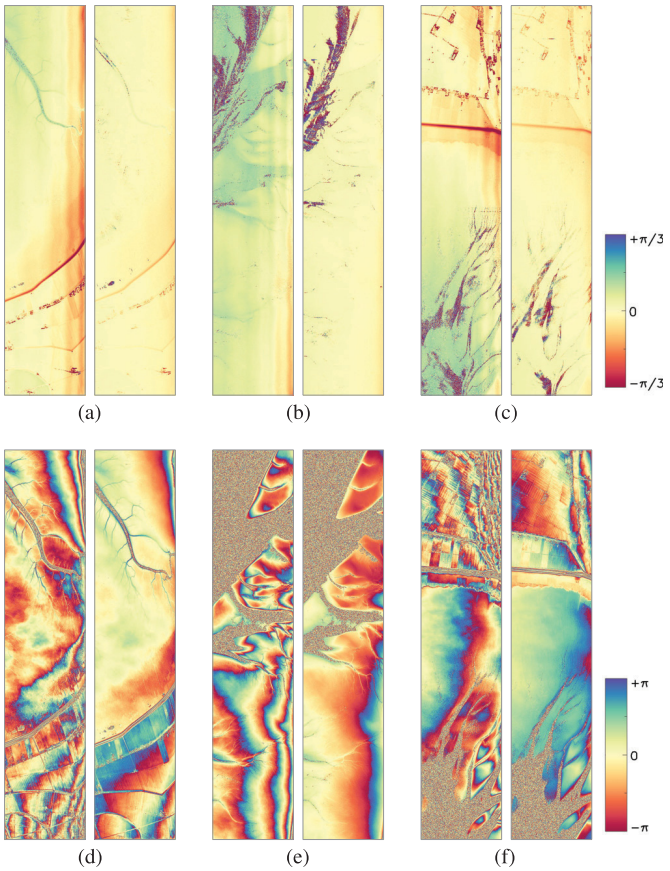

Fig. 28. Estimated wrapped phases from all X- and S-band single- and repeat-pass interferograms. The single-pass phases are scaled from $-\pi/3$ to $\pi/3$, and the repeat-pass phases are scaled from $-\pi$ to π. (a) (Left) X- and (Right) S-band single-pass interferometric phase, first tile. (b) (Left) X- and (Right) S-band single-pass interferometric phase, second tile. (c) (Left) X- and (Right) S-band single-pass interferometric phase, third tile. (d) (Left) X- and (Right) S-band repeat-pass interferometric phase, first tile. (e) (Left) X- and (Right) S-band repeat-pass interferometric phase, second tile. (f) (Left) X- and (Right) S-band repeat-pass interferometric phase, third tile.

are shown in the first row of Fig. 28, while the repeat-pass residual phases are shown in the second row. For a better visualization, the figures were divided in tiles whose locations can be seen in Fig. 27. Note that the information over flooded areas (upper part of tile 2 and lower part of tile 3) is virtually lost in the repeat-pass interferograms due to the strong temporal decorrelation but can be partially recovered with the single-pass data. Moreover, note that Fig. 27 shows the results before any multipath correction has been applied. Hence, range undulations can be clearly seen in the single-pass phases.

S- and X-band elevation models were generated using the suggested chain (see Fig. 2) and considering the algorithms proposed in Sections IV–VIII, i.e., no dual-frequency fusion has been applied. The results are shown at the top and bottom of Fig. 29. A water mask computed from the repeat-pass coherences and amplitudes has been applied to the results.

The obtained DEMs are compared with an ALS reference to evaluate the achieved relative and absolute vertical accuracies. The available laser data were acquired three months prior to the SAR data, and both F-SAR DEM and the ALS reference

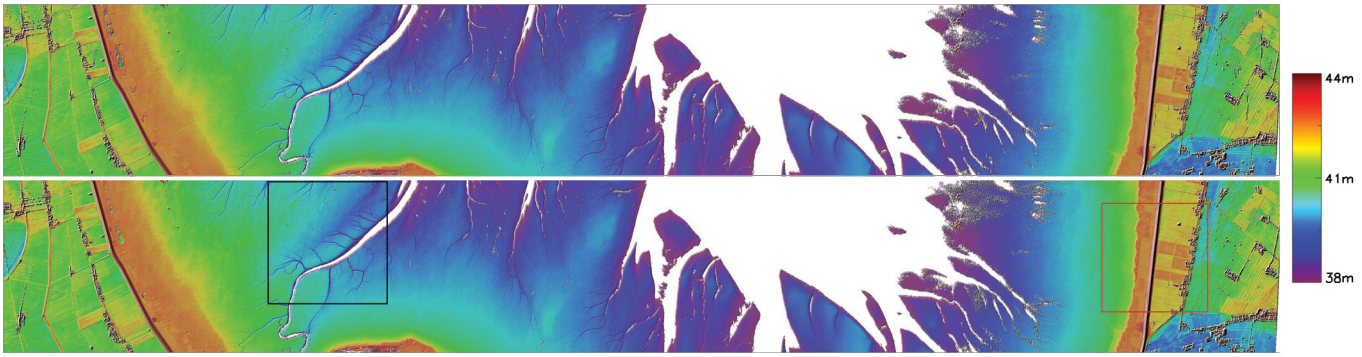

Fig. 29. Surface models of the Jade Bight obtained with (Top) S-band and (Bottom) X-band data. Both DEMs are geocoded in a UTM grid with 1 m × 1 m posting. The black and red rectangles highlight ROIs for further evaluation.

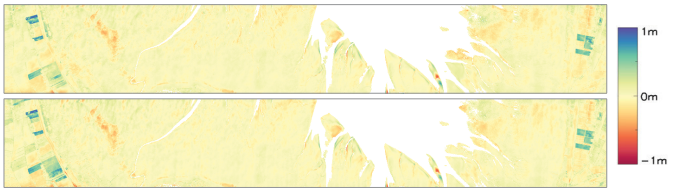

Fig. 30. Differences between the F-SAR and ALS elevation models. The first row gives the S-band comparison, while X-band one appears in the second row. The differences are scaled from −1 to 1 m and show good agreement between the obtained DEM and the reference.

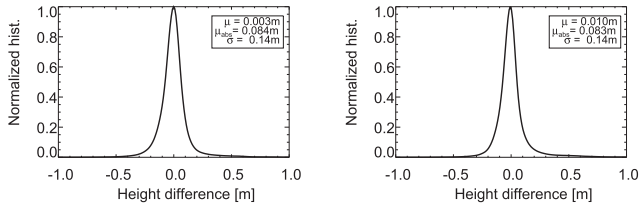

Fig. 31. Histograms of the differences between (Left) S-band F-SAR and ALS elevation models and (Right) X-band F-SAR and ALS elevation models.

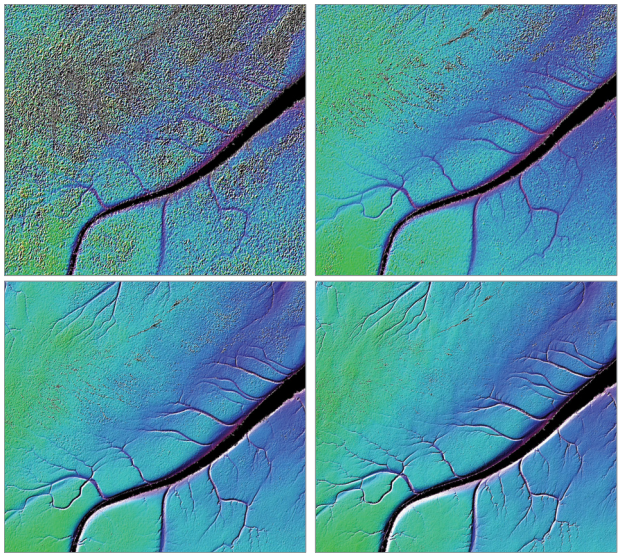

Fig. 32. Shaded relief images corresponding to the F-SAR elevation models of the first ROI. The first row shows (Left) S-band and (Right) X-band single-pass elevation models. The second row shows (Left) S-band and (Right) X-band repeat-pass elevation models. Tidal channels are resolved in all the F-SAR DEM with the X-band repeat-pass DEM presenting the finest detail content.

were constructed in a UTM grid with 1 m × 1 m posting. The first row of Fig. 30 shows the difference between the S-band and ALS models, while the second row gives the difference between the X-band and ALS models. Overall, good agreement is observed between the generated models and the reference. This attests for the good performance not only of the baseline calibration methodology suggested in Section VI but also of the filtering approach presented in Section VIII, which is able to reduce low-pass errors of up to 3 m in the original repeat-pass data sets down to centimeters.

A quantitative analysis of the achieved accuracies is obtained from the histograms of the height differences. Fig. 31 shows the histogram of the difference between S-band DEM and the reference (left) and the histogram of the difference between X-band DEM and reference (right). The histograms are similar and show an overall mean difference around 0 m and a mean absolute difference of less than 10 cm. Note that due to residual low-pass frequency disturbances and differences in vegetation height between the F-SAR and the references models, the histograms are slightly skewed, causing the slightly higher mean absolute deviation. In both cases, the standard deviation is around 14 cm.

In the following, two ROIs are evaluated in order to give a qualitative measurement of the level of detail contained in the F-SAR elevation models. The locations of the ROIs are indicated in Fig. 29 by the black and red rectangles.

The first ROI (black rectangle in Fig. 29) encompasses the bight surface and tidal channels in the middle-western part of the scene. Shaded relief images of the correspondent F-SAR models are given in Fig. 32, where S- and X-band single-pass DEMs appear in the first row and S- and X-band repeat-pass DEMs are given in the second row. Many fine branches are visible in both F-SAR repeat-pass DEMs. Furthermore, it can be seen that the best result is obtained with the X-band repeat-pass model, while both single-pass models present considerably higher noise levels. The statistics of the ROI are evaluated through the plots in Fig. 33.

The second ROI (red rectangle in Fig. 29) is chosen in the eastern side of the scene, and includes part of the bight, the dike, vegetated areas, and a few buildings. Shaded relief

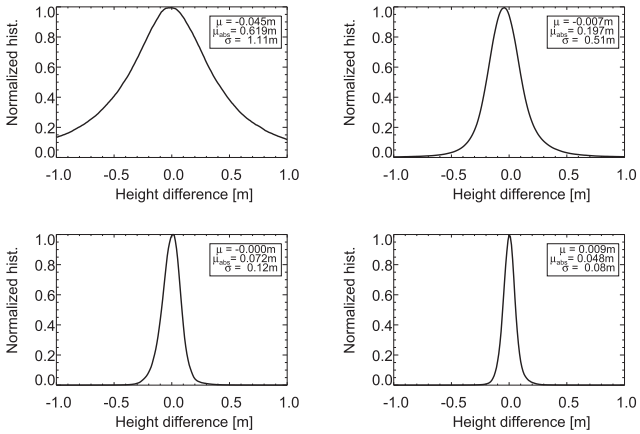

Fig. 33. Histograms of the height differences between the F-SAR and ALS elevation models corresponding to the first ROI. The first row shows (Left) S-band and (Right) X-band single-pass results, while the second row shows (Left) S-band and (Right) X-band repeat-pass results.

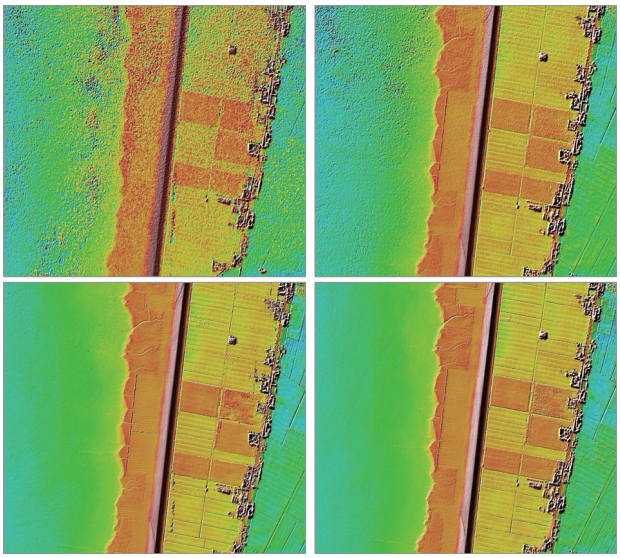

Fig. 34. Shaded relief images corresponding to the F-SAR elevation models of the second ROI. The first row shows (Left) S-band and (Right) X-band single-pass elevation models. The second row shows (Left) S-band and (Right) X-band repeat-pass elevation models. Fine features can be distinguished in both bight and vegetated areas.

images of the F-SAR elevation models are given in Fig. 34. Again, S- and X-band single-pass DEMs appear in the first row, and S- and X-band repeat-pass DEMs in the second one. In all the images, fine features can be distinguished in both bight and vegetated areas. Also in this example, the superiority of the repeat-pass products over the single-pass ones is clear. Note that this ROI contains agricultural fields not present in the laser DEM. Hence, larger inconsistencies are expected when directly comparing the reference and F-SAR elevation models. This is readily seen in the histograms of the height differences shown in Fig. 35. Both repeat-pass distributions contain a sidelobe around the mean vegetation height of the fields. The sidelobe is still recognizable in the X-band single-pass histogram, but it is lost in the S-band single-pass result due to the increased noise content. For this ROI, the standard deviation of the height difference should be interpreted with caution, since it incorporates not only the errors in the F-SAR DEM but also the disparity of the topographic content.

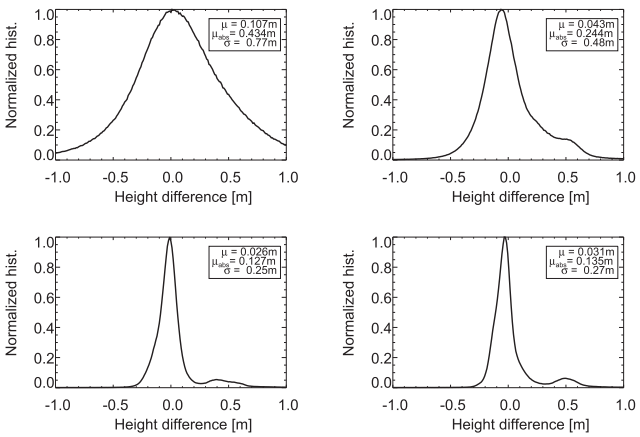

Fig. 35. Histograms of the height differences between the F-SAR and ALS elevation models for the second ROI. The first row shows (Left) S-band and (Right) X-band single-pass results, while the second row shows (Left) S-band and (Right) X-band repeat-pass results. Due to the presence of agricultural fields with tall crops (not included in the ALS reference), larger inconsistencies are observed.

Fig. 36. Difference between F-SAR S- and X-band DEMs, scaled from −0.5 to 0.5 m. The image shows that differences in penetration between S- and X-bands are below a few centimeters for the majority of the scene, and cause the height differences of around 30 cm for areas with short vegetation.

Differences in penetration between X- and S-band waves are negligible for the majority of this particular scene. Nevertheless, a few agricultural fields present different topographies in the two generated DEMs. This can be observed in Fig. 36, which depicts the difference between S- and X-band F-SAR elevation models, scaled from −0.5 to 0.5 m. The image shows that the absolute height difference for vegetated areas is around 30 cm. As expected, in such regions, the X-band DEM is higher than the S-band one.

Since the main goal of this experiment is to map the bight area, it is reasonable to merge X- and S-bands into a final elevation DEM with an improved relative accuracy, as explained in Section IX. The wavelet fusion scheme proposed in this paper was performed to combine X- and S-band data into a final elevation model, neglecting possible differences in penetration [i.e., using (70)–(75)]. Figs. 37 and 38 show the resulting shaded relief images of the selected ROIs located at the middle-western and eastern portion of the bight, respectively. In Figs. 37 and 38, the DEM presented in the left was constructed by a simple ML estimation, while the one in the right was generated with the proposed approach. Visually, the ML DEM does not show much improvement in comparison with the X-band elevation models in Figs. 32 and 34. In fact, since the quality of the X-band repeat-pass data is considerably higher, it dominates the resulting DEM. On the other hand, a quality improvement of the bight terrain estimation is observed with the wavelet-domain fusion, which yields a better regularization (i.e., noise removal), specially within the bight area.

Figs. 39 and 40 show the histograms of the differences between the final DEM and the ALS reference within the

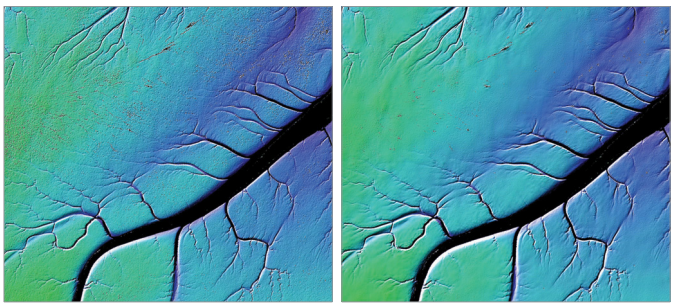

Fig. 37. Shaded relief images of the first ROI. Both results are the combinations of X- and S-band elevation models. For the DEM presented in (Left), an ML estimation was performed, while for the one in (Right), the wavelet-domain fusion was performed.

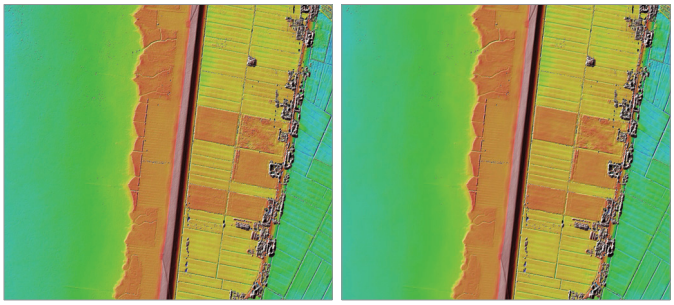

Fig. 38. Shaded relief images of the second ROI. Both results are the combinations of X- and S-band elevation models. For the DEM presented in (Left), an ML estimation was performed, while for the one in (Right), the wavelet-domain fusion was performed.

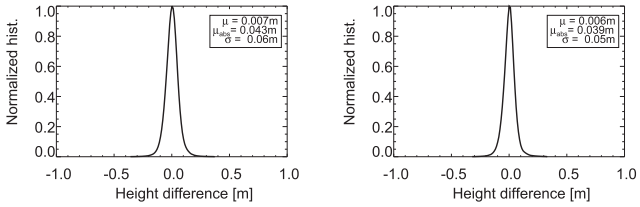

Fig. 39. Histograms of the height differences between F-SAR final DEM and ALS reference for the first ROI. (Left) ML estimation. (Right) Proposed wavelet fusion approach.

selected ROI. In both cases, Figs. 39 and 40 (left) correspond to the DEM estimated with the ML algorithm, while Figs. 39 and 40 (right) correspond to the results with the proposed wavelet fusion. For both ROIs, the two estimation strategies yield a small decrease in the height standard deviation in comparison to the X-band DEM (from 0.08 to 0.06 m and 0.05 m, for the first ROI and from 0.27 to 0.24 m and 0.23 m for the second ROI). The small reduction in the standard deviation indicates that the main sources of discrepancies are residual low-pass disturbances in the SAR products and residual errors in the ALS reference.

Finally, Fig. 41 shows the profiles of the final DEM along the (left) North and (right) East directions. The profiles were extracted from the first ROI, i.e., they correspond to intertidal mudflats including several water tidal channels. The result of the ML estimation is shown in black curve, the result considering the wavelet reconstruction appears in red curve, and the MAP+TV regularization appears in blue curve. The profiles show that both wavelet and MAP+TV reconstructions are able to reduce the noise while also fairly recovering small

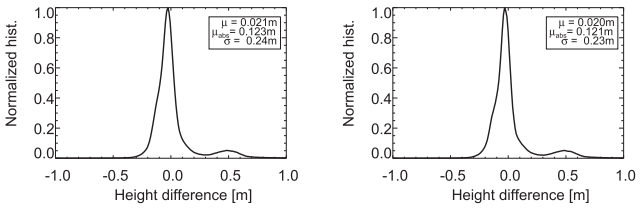

Fig. 40. Histograms of the height differences between F-SAR final DEM and ALS reference for the second ROI. (Left) ML estimation. (Right) Proposed wavelet fusion approach.

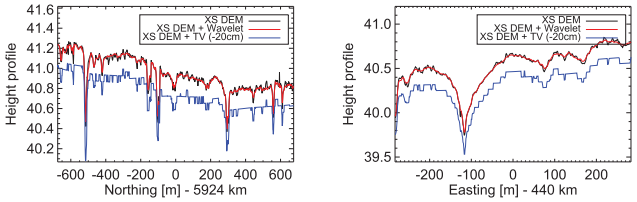

Fig. 41. Profiles of the F-SAR final DEM along the (Left) North and (Right) East directions. In both cases, the result of the ML estimation is shown in black curve, the result considering wavelet reconstruction appears in red curve, and the MAP+TV regularization appears in blue curve. An offset of 20 cm has been introduced in the MAP+TV regularization result in order to improve visualization.

features. The blocking artifacts in the blue curve are due to the nature of the TV regularization [109], and can be avoided by using higher order priors.

XI. Conclusion

In this paper, a methodology to generate highly accurate elevation maps from large-baseline airborne InSAR data has been described. The procedure uses DFDB data sets to ensure the relative and absolute height accuracy of the derived model. This combination profits from the stability of single-pass interferograms in relation to slowly varying errors and the low noise sensitivity associated with large-baseline elevation models.

Specifically, the dual-frequency redundancy is exploited in the phase unwrapping, unwrapping error correction, baseline calibration, and regularization steps. On the other hand, the unbiased single-pass information mainly supports the correction of low-frequency disturbances and absolute calibration of the repeat-pass data. Moreover, the single-pass elevation models can be used to fill the gaps corresponding to areas where the repeat-pass interferograms are completely decorrelated, typically the case of volume scatterers.

The strength of the DFDB configuration is the exploitation of the consistence between the data sets. Hence, its use is not suitable when the penetration differences between the X- and S-band waves are large, which might occur, e.g., when imaging terrain covered with snow or glaciers. In such cases, an alternative to promote proper unwrapping is to use smaller baselines in order to ensure that the penetration differences are smaller than the HoAs. Alternatively, we can replace the S-band data set for a second X-band one with a smaller baseline. In this case, the baselines should be such that the corresponding HoA is larger than the expected residual low-pass errors, thus also resulting in decreased relative height accuracy. Moreover, both solutions will also lead to degraded absolute referencing due to the suboptimal calibration caused

by inconsistency between the data sets (differences in the phase centers or differences between low-pass artifacts).

Although the DEM generation chain was derived for the DFDB configuration, modifications can be performed according to the available data, and the proposed algorithms can be used according to the characteristics of the specific configurations and systems. As mentioned earlier, it can be adopted for data from a single-frequency/dual-baseline configuration, albeit with an overall performance loss. In another example, if a simultaneous acquisition with different carrier frequencies is not viable, a dual-frequency configuration can be emulated by splitting the range spectrum of a single data set into two subbands, provided the bandwidth of the system allows, as suggested in [13] and [110]. Also, depending on the required accuracy, the role of the single-pass data to support calibration can be fulfilled by external references, e.g., the TanDEM-X global DEM.

The efficiency of the DFDB configuration and proposed chain has been validated with airborne SAR data of an experiment conducted in Germany with the F-SAR sensor over tidal flats in the Jade Bight in the North Sea, consisting of two passes separated by an effective baseline of around 30 m, each one acquiring data simultaneously in X- and S-bands. The proposed algorithms allowed the generation of elevation models with vertical relative and absolute accuracies in the order of centimeters in a 1 m × 1 m spatial grid, unprecedented results for the F-SAR sensor. Although the data used for the validation are flat, a good performance is also expected for steep terrain. Note that the proposed calibration approaches are fairly robust to topography, since they rely on phase differences. Moreover, the suggested fusion strategy mainly exploits the consistency between X- and S-band data, thus not assuming smooth terrain. The critical step for such scenarios would be the phase unwrapping. In fact, the dual-channel unwrapping strategy discussed in Section IV also performs well for complex scene, as shown in [36] using TanDEM-X large-baseline data acquired over the Atacama desert/mountains. Moreover, remaining unwrapping errors can be corrected by the active-contour-based strategy proposed here (also based on phase differences), provided that the accuracy of available reference DEMs (e.g., the TanDEM-X DEM) is good enough to allow for the verification of single-pass data sets.

APPENDIX

This section provides the solution of the minimization problem defined for identifying unwrapping errors in X- and S-band repeat-pass phases. Writing the global functional as

$$F_\varepsilon(\boldsymbol{\Theta}) = \sum_{l=1}^{6} \xi_l \int_\Omega \mathcal{L}_{\varepsilon,l}\left(x, y, \boldsymbol{\Theta}, \frac{\partial \boldsymbol{\Theta}}{\partial x}, \frac{\partial \boldsymbol{\Theta}}{\partial y}\right) dxdy \quad (80)$$

where $\boldsymbol{\Theta} = [\Theta_1 \ldots, \Theta_K]$, and being the Euler–Lagrange equation associated with each functional $F_{\varepsilon,k}$ and Θ_i

$$\frac{\partial F_{\varepsilon,k}}{\partial \Theta_i} = \frac{\partial \mathcal{L}_{\varepsilon,k}}{\partial \Theta_i} - \frac{\partial}{\partial x}\frac{\partial \mathcal{L}_{\varepsilon,k}}{\partial \frac{\partial \Theta_i}{\partial x}} - \frac{\partial}{\partial y}\frac{\partial \mathcal{L}_{\varepsilon,k}}{\partial \frac{\partial \Theta_i}{\partial y}} = 0 \quad (81)$$

the final system of coupled PDEs used for the evolution is given by

$$\begin{aligned}\frac{\partial F_\varepsilon}{\partial \Theta_i} &= \xi_1 \delta_\varepsilon(\Theta_i)\left(\sum_i^K H_\varepsilon(\Theta_i) - 1\right) \\ &+ \xi_2 \delta_\varepsilon(\Theta_i)\left(\frac{u_{\mathrm{X}} - 2\pi n_{\mathrm{err}\,i}^{\mathrm{X_{RP}}}}{\sigma_{\mathrm{X}}}\right)^2 \\ &+ \xi_3 \delta_\varepsilon(\Theta_i)\left(\frac{u_{\mathrm{S}} - 2\pi n_{\mathrm{err}\,i}^{\mathrm{S_{RP}}}}{\sigma_{\mathrm{S}}}\right)^2 \\ &+ \xi_4 \delta_\varepsilon(\Theta_i)\left(\frac{u_{\mathrm{S}} - 2\pi n_{\mathrm{err}\,i}^{\mathrm{S_{RP}}}\left(u_{\mathrm{X}} - 2\pi n_{\mathrm{err}\,i}^{\mathrm{X_{RP}}}\right)\cdot \frac{k_{z,\mathrm{real}}^{S_{\mathrm{RP}}}}{k_{z,\mathrm{real}}^{X_{\mathrm{RP}}}}}{\sigma_{\mathrm{SX}}}\right)^2 \\ &- \xi_5 g\left(\phi_{\mathrm{res}}^{\mathrm{X_{RP}}}, \phi_{\mathrm{res}}^{\mathrm{S_{RP}}}\right)\delta_\varepsilon(\Theta_i)\mathrm{div}\left(\frac{\nabla \Theta_{\mathrm{i}}}{|\nabla \Theta_{\mathrm{i}}|}\right) \\ &- \xi_6 \delta_\varepsilon(\Theta_i)\mathrm{div}\left(\frac{\nabla \Theta_i}{|\nabla \Theta_i|}\right) \end{aligned} \quad (82)$$

where $g()$ assumes zero on edges and a positive value otherwise, example

$$\begin{aligned} &g\left(\phi_{\mathrm{res}}^{\mathrm{X_{SP}}}, \phi_{\mathrm{res}}^{\mathrm{S_{SP}}}\right) \\ &= \frac{1}{1 + \left|\nabla\left(G \circledast \phi_{\mathrm{res}}^{\mathrm{X_{SP}}}\right)\right|^p + \left|\nabla\left(G \circledast \phi_{\mathrm{res}}^{\mathrm{S_{SP}}}\right)\right|^p}, \quad p \geqslant 1 \end{aligned} \quad (83)$$

and the continuous approximations of the Heaviside and Dirac delta measures are given by [76]

$$H_\varepsilon \to H, \quad \text{as } \varepsilon \to 0^+ \quad (84)$$

and

$$\delta_\varepsilon \to \delta, \quad \text{as } \varepsilon \to 0^+. \quad (85)$$

As in the original classification in [75], (82) is embedded in an iterative scheme such that

$$\begin{aligned}\Theta_i^{t+1} &= \Theta_i^t \\ &- dt\{\delta_\varepsilon(\Theta_i)[\xi_1(\sum_i^K H(\Theta_i) - 1) \\ &+ \xi_2\left(\frac{u_{\mathrm{X}} - 2\pi n_{\mathrm{err}\,i}^{\mathrm{X_{RP}}}}{\sigma_{\mathrm{X}}}\right)^2 + \xi_3\left(\frac{u_{\mathrm{S}} - 2\pi n_{\mathrm{err}\,i}^{\mathrm{S_{RP}}}}{\sigma_{\mathrm{S}}}\right)^2 \\ &+ \xi_4\left(\frac{u_{\mathrm{S}} - 2\pi n_{\mathrm{err}\,i}^{\mathrm{S_{RP}}} - \left(u_{\mathrm{X}} - 2\pi n_{\mathrm{err}\,i}^{\mathrm{X_{RP}}}\right)\cdot \frac{k_{z,\mathrm{real}}^{S_{\mathrm{RP}}}}{k_{z,\mathrm{real}}^{X_{\mathrm{RP}}}}}{\sigma_{\mathrm{SX}}}\right)^2 \\ &- \xi_5 g\left(\phi_{\mathrm{res}}^{\mathrm{X_{RP}}}, \phi_{\mathrm{res}}^{\mathrm{S_{RP}}}\right)\mathrm{div}\left(\frac{\nabla \Theta_{\mathrm{i}}}{|\nabla \Theta_{\mathrm{i}}|}\right) - \xi_6 \mathrm{div}\left(\frac{\nabla \Theta_{\mathrm{i}}}{|\nabla \Theta_{\mathrm{i}}|}\right)\Big]\Big\}. \end{aligned} \quad (86)$$

The initialization is performed by simply applying the signed distance function to initial unwrapping error maps, e.g., the ones obtained with (40). The evolution of (86) is then alternate with the reinitialization

$$\begin{aligned} \Lambda_i^0 &= \Theta_i^{t+1} \\ \Lambda_i^{\tau+1} &= \Lambda_i^\tau - dt\left(\mathrm{sign}\left(\Lambda_i^0\right)\left[1 - \left|\nabla \Lambda_i^\tau\right|\right]\right) \end{aligned} \quad (87)$$

until no further changes are observed in the region interfaces.

REFERENCES

[1] H. A. Zebker and R. M. Goldstein, "Topographic mapping from interferometric synthetic aperture radar observations," *J. Geophys. Res.*, vol. 91, no. 5, pp. 4993–4999, 1986.

[2] A. K. Gabriel and R. M. Goldstein, "Crossed orbit interferometry: Theory and experimental results from SIR-B," *Int. J. Remote Sens.*, vol. 9, no. 5, pp. 857–872, 1988.

[3] M. Eineder *et al.*, "Analysis of SRTM interferometric X-band data: First results," in *Proc. IEEE Int. Geosci. Remote Sens. Symp. (IGARSS)*, vol. 6. Jul. 2000, pp. 2593–2595.

[4] G. Krieger *et al.*, "TanDEM-X: A satellite formation for high-resolution SAR interferometry," *IEEE Trans. Geosci. Remote Sens.*, vol. 45, no. 11, pp. 3317–3341, Nov. 2007.

[5] C. Magnard, M. Frioud, D. Small, T. Brehm, and E. Meier, "Analysis of a maximum likelihood phase estimation method for airborne multibaseline SAR interferometry," *IEEE J. Sel. Topics Appl. Earth Observ. Remote Sens.*, vol. 9, no. 3, pp. 1072–1085, Mar. 2016.

[6] S. Perna *et al.*, "The InSAeS4 airborne X-band interferometric SAR system: A first assessment on its imaging and topographic mapping capabilities," *Remote Sens.*, vol. 8, no. 1, p. 40, 2016.

[7] A. Reigber, "Range dependent spectral filtering to minimize the baseline decorrelation in airborne SAR interferometry," in *Proc. IEEE Int. Geosci. Remote Sens. Symp. (IGARSS)*, vol. 3. Jun./Jul. 1999, pp. 1721–1723.

[8] D. C. Ghiglia and D. E. Wahl, "Interferometric synthetic aperture radar terrain elevation mapping from multiple observations," in *Proc. IEEE 6th Digit. Signal Process. Workshop*, Oct. 1994, pp. 33–36.

[9] W. Xu, E. C. Chang, L. K. Kwoh, H. Lim, W. Cheng, and A. Heng, "Phase-unwrapping of SAR interferogram with multi-frequency or multi-baseline," in *Proc. IEEE Int. Geosci. Remote Sens. Symp. (IGARSS)*, vol. 2. Aug. 1994, pp. 730–732.

[10] A. Ferretti, A. M. Guarnieri, C. Prati, and F. Rocca, "Multi-baseline interferometric techniques and applications," in *Proc. ERS SAR Interferometry*, vol. 406. 1997, p. 243.

[11] K. Schmitt and W. Wiesbeck, "An interferometric SAR processor avoiding phase ambiguities," in *Proc. IEEE Int. Geosci. Remote Sens. Symp. (IGARSS)*, vol. 4. Aug. 1997, pp. 1713–1715.

[12] J. Allievi, A. Ferretti, C. Prati, R. Ratti, and F. Rocca, "Automation of the DEM reconstruction from ERS Tandem pairs," in *Proc. IEEE Int. Geosci. Remote Sens. Symp. (IGARSS)*, vol. 6. Jul. 2001, pp. 2504–2506.

[13] V. Pascazio and G. Schirinzi, "Estimation of terrain elevation by multifrequency interferometric wide band SAR data," *IEEE Signal Process. Lett.*, vol. 8, no. 1, pp. 7–9, Jan. 2001.

[14] M. Eineder and N. Adam, "A maximum-likelihood estimator to simultaneously unwrap, geocode, and fuse SAR interferograms from different viewing geometries into one digital elevation model," *IEEE Trans. Geosci. Remote Sens.*, vol. 43, no. 1, pp. 24–36, Jan. 2005.

[15] G. Fornaro *et al.*, "Maximum likelihood multi-baseline SAR interferometry," *IEE Proc.-Radar Sonar Navigat.*, vol. 153, no. 3, pp. 279–288, Dec. 2006.

[16] M. Schmitt and U. Stilla, "Maximum-likelihood estimation for multi-aspect multi-baseline SAR interferometry of urban areas," *ISPRS J. Photogramm. Remote Sens.*, vol. 87, pp. 68–77, Jan. 2014.

[17] V. Pascazio and G. Schirinzi, "Multifrequency InSAR height reconstruction through maximum likelihood estimation of local planes parameters," *IEEE Trans. Image Process.*, vol. 11, no. 12, pp. 1478–1489, Dec. 2002.

[18] G. Ferraiuolo, V. Pascazio, and G. Schirinzi, "Maximum *a posteriori* estimation of height profiles in InSAR imaging," *IEEE Geosci. Remote Sens. Lett.*, vol. 1, no. 2, pp. 66–70, Apr. 2004.

[19] G. Ferraioli, A. Shabou, F. Tupin, and V. Pascazio, "Fast InSAR multichannel phase unwrapping for DEM generation," in *Proc. Joint Urban Remote Sens. Event*, May 2009, pp. 1–6.

[20] A. Shabou, F. Baselice, and G. Ferraioli, "Urban digital elevation model reconstruction using very high resolution multichannel InSAR data," *IEEE Trans. Geosci. Remote Sens.*, vol. 50, no. 11, pp. 4748–4758, Nov. 2012.

[21] F. Baselice, G. Ferraioli, V. Pascazio, and G. Schirinzi, "Contextual information-based multichannel synthetic aperture radar interferometry: Addressing DEM reconstruction using contextual information," *IEEE Signal Process. Mag.*, vol. 31, no. 4, pp. 59–68, Jul. 2014.

[22] C.-A. Deledalle, L. Denis, G. Ferraioli, and F. Tupin, "Combining patch-based estimation and total variation regularization for 3D InSAR reconstruction," in *Proc. IEEE Int. Geosci. Remote Sens. Symp. (IGARSS)*, Jul. 2015, pp. 2485–2488.

[23] M. Hubig, S. Suchandt, and M. Eineder, "Automatic correction of baseline and phase unwrapping errors in SAR interferograms," in *Proc. 3rd Eur. Conf. Synth. Aperture Radar*, May 2000, pp. 1–4.

[24] J. J. Mohr and J. P. M. Boncori, "An error prediction framework for interferometric SAR data," *IEEE Trans. Geosci. Remote Sens.*, vol. 46, no. 6, pp. 1600–1613, Jun. 2008.

[25] M. Lachaise, T. Fritz, and R. Bamler, "The dual-baseline phase unwrapping correction framework for the TanDEM-X mission part 1: Theoretical description and algorithms," *IEEE Trans. Geosci. Remote Sens.*, vol. 56, no. 2, pp. 780–798, Feb. 2017. [Online]. Available: http://elib.dlr.de/114163/

[26] G. Ferraioli, G. Ferraiuolo, and V. Pascazio, "Phase-offset estimation in multichannel SAR interferometry," *IEEE Geosci. Remote Sens. Lett.*, vol. 5, no. 3, pp. 458–462, Jul. 2008.

[27] J. C. Mura, M. Pinheiro, R. Rosa, and J. Moreira, "A phase-offset estimation method for InSAR DEM generation based on phase-offset functions," *Remote Sens.*, vol. 4, no. 3, pp. 745–761, 2012.

[28] S. Perna, C. Esposito, P. Berardino, A. Pauciullo, C. Wimmer, and R. Lanari, "Phase offset calculation for airborne InSAR DEM generation without corner reflectors," *IEEE Trans. Geosci. Remote Sens.*, vol. 53, no. 5, pp. 2713–2726, May 2015.

[29] C. Esposito, A. Pauciullo, P. Berardino, R. Lanari, and S. Perna, "A simple solution for the phase offset estimation of airborne SAR interferograms without using corner reflectors," *IEEE Geosci. Remote Sens. Lett.*, vol. 14, no. 3, pp. 379–383, Mar. 2017.

[30] M. Pinheiro, A. Reigber, and J. Lloredo, "Improving satellite derived DEMS by using airborne InSAR data: The TanDEM-X/F-SAR case of study," in *Proc. IEEE Int. Geosci. Remote Sens. Symp. (IGARSS)*, Jul. 2015, pp. 3834–3837.

[31] C. Magnard, M. Frioud, D. Small, T. Brehm, H. Essen, and E. Meier, "Processing of MEMPHIS Ka-band multibaseline interferometric SAR data: From raw data to digital surface models," *IEEE J. Sel. Topics Appl. Earth Observ. Remote Sens.*, vol. 7, no. 7, pp. 2927–2941, Jul. 2014.

[32] G. Krieger *et al.*, "TanDEM-X: A radar interferometer with two formation-flying satellites," *Acta Astron.*, vol. 89, pp. 83–98, Aug./Sep. 2013.

[33] X. Gao, Y. Liu, T. Li, and D. Wu, "High precision DEM generation algorithm based on InSAR multi-look iteration," *Remote Sens.*, vol. 9, no. 7, p. 741, 2017.

[34] I. Hajnsek and T. Busche, "TanDEM-X: Science activities," in *Proc. 10th Eur. Conf. Synth. Aperture Radar (EUSAR)*, Jun. 2014, pp. 1–3.

[35] S.-K. Lee and J.-H. Ryu, "High-accuracy tidal flat digital elevation model construction using TanDEM-X science phase data," *IEEE J. Sel. Topics Appl. Earth Observ. Remote Sens.*, vol. 10, no. 6, pp. 2713–2724, Jun. 2017.

[36] M. Pinheiro, A. Reigber, and A. Moreira, "Large-baseline InSAR for precise topographic mapping: A framework for TanDEM-X large-baseline data," *Adv. Radio Sci.*, vol. 15, pp. 231–241, Sep. 2017. [Online]. Available: https://www.adv-radio-sci.net/15/231/2017/

[37] A. Wehr and U. Lohr, "Airborne laser scanning—An introduction and overview," *ISPRS J. Photogram. Remote Sens.*, vol. 54, nos. 2–3, pp. 68–82, Jul. 1999.

[38] J. Shan and S. Aparajithan, "Urban DEM generation from raw LiDAR data," *Photogramm. Eng. Remote Sens.*, vol. 71, no. 2, pp. 217–226, 2005.

[39] X. Liu, "Airborne LiDAR for DEM generation: Some critical issues," *Prog. Phys. Geogr.*, vol. 32, no. 1, pp. 31–49, 2008.

[40] H. Yu, X. Lu, X. Ge, and G. Cheng, "Digital terrain model extraction from airborne LiDAR data in complex mining area," in *Proc. 18th Int. Conf. Geoinform.*, Jun. 2010, pp. 1–6.

[41] K. A. C. D. Macedo, C. Wimmer, and J. R. Moreira, "Highly accurate and precise airborne single-pass interferometry for DEM generation over challenging terrain," in *Proc. IEEE Int. Geosci. Remote Sens. Symp. (IGARSS)*, Jul. 2014, pp. 394–397.

[42] L. Marotti, A. Meta, and A. Coccia, "MetaSensing airborne radar: X- and Ku-band single-pass digital surface model generation," in *Proc. IEEE 5th Asia–Pacific Conf. Synth. Aperture Radar (APSAR)*, Sep. 2015, pp. 184–186.

[43] A. Reigber *et al.*, "Very-high-resolution airborne synthetic aperture radar imaging: Signal processing and applications," *Proc. IEEE*, vol. 101, no. 3, pp. 759–783, Mar. 2013.

[44] T. Fritz, U. Balss, R. Bamler, and M. Eineder, "Phase unwrapping correction with dual-baseline data for the TanDEM-X mission," in *Proc. IEEE Int. Geosci. Remote Sens. Symp. (IGARSS)*, Jul. 2012, pp. 5566–5569.

[45] M. Pinheiro, P. Prats, R. Scheiber, and J. Fischer, "Multi-path correction model for multi-channel airborne SAR," in *Proc. IEEE Int. Geosci. Remote Sens. Symp. (IGARSS)*, vol. 3. Jul. 2009, pp. 729–732.

[46] Y. Mao, M. Xiang, L. Wei, and S. Han, "The mathematic model of multipath error in airborne interferometric SAR system," in *Proc. IEEE Int. Geosci. Remote Sens. Symp. (IGARSS)*, Jul. 2010, pp. 2904–2907.

[47] J. Dall, "Cross-calibration of interferometric SAR data," *IEE Proc.-Radar, Sonar Navigat.*, vol. 150, no. 3, pp. 177–183, Jun. 2003.

[48] M. Pinheiro, R. Scheiber, and A. Reigber, "Combination of repeat and single-pass dual-frequency airborne InSAR data for accurate height estimation," in *Proc. IEEE Int. Geosci. Remote Sens. Symp. (IGARSS)*, Jul. 2014, pp. 2237–2240.

[49] R. Bamler and P. Hartl, "Synthetic aperture radar interferometry," *Inverse Problems*, vol. 14, no. 4, pp. R1–R54, 1998.

[50] A. Moreira, P. Prats-Iraola, M. Younis, G. Krieger, I. Hajnsek, and K. P. Papathanassiou, "A tutorial on synthetic aperture radar," *IEEE Geosci. Remote Sens. Mag.*, vol. 1, no. 1, pp. 6–43, Mar. 2013.

[51] P. Prats and J. J. Mallorqui, "Estimation of azimuth phase undulations with multisquint processing in airborne interferometric SAR images," *IEEE Trans. Geosci. Remote Sens.*, vol. 41, no. 6, pp. 1530–1533, Jun. 2003.

[52] A. Danklmayer, B. J. Doring, M. Schwerdt, and M. Chandra, "Assessment of atmospheric propagation effects in SAR images," *IEEE Trans. Geosci. Remote Sens.*, vol. 47, no. 10, pp. 3507–3518, Oct. 2009.

[53] M. Jaeger, R. Scheiber, and A. Reigber, "External calibration of multi-channel SAR sensors based on the pulse-by-pulse analysis of range compressed data," in *Proc. EUSAR*, 2018, pp. 1–4.

[54] A. Reigber, P. Prats, and J. J. Mallorqui, "Refined estimation of time-varying baseline errors in airborne SAR interferometry," *IEEE Geosci. Remote Sens. Lett.*, vol. 3, no. 1, pp. 145–149, Jan. 2006.

[55] W. Xu and I. Cumming, "A region-growing algorithm for InSAR phase unwrapping," *IEEE Trans. Geosci. Remote Sens.*, vol. 37, no. 1, pp. 124–134, Jan. 1999.

[56] E. L. Christensen and M. Dich, "SAR antenna design for ambiguity and multipath suppression," in *Proc. IEEE Int. Geosci. Remote Sens. Symp. (IGARSS)*, Aug. 1993, pp. 784–787.

[57] S. N. Madsen, N. Skou, K. Woelders, and J. Granholm, "EMISAR single pass topographic SAR interferometer modes," in *Proc. IEEE Int. Geosci. Remote Sens. Symp. (IGARSS)*, vol. 1. May 1996, pp. 674–676.

[58] J. Dall, J. Grinder-Pedersen, and S. N. Madsen, "Calibration of a high resolution airborne 3D SAR," in *Proc. IEEE Int. Geosci. Remote Sens. (IGARSS) Remote Sens.-A Sci. Vis. Sustain. Develop.*, vol. 2. Aug. 1997, pp. 1018–1021.

[59] Y. Kobayashi, K. Sarabandi, L. Pierce, and M. C. Dobson, "An evaluation of the JPL TOPSAR for extracting tree heights," *IEEE Trans. Geosci. Remote Sens.*, vol. 38, no. 6, pp. 2446–2454, Nov. 2000.

[60] E. Chapin, S. Hensley, and T. R. Michel, "Calibration of an across track interferometric P-band SAR," in *Proc. IEEE Int. Geosci. Remote Sens. Symp. (IGARSS)*, vol. 1. Jul. 2001, pp. 502–504.

[61] M. Limbach, B. Gabler, A. D. Maria, R. Horn, and A. Reigber, "DLR compact test range facility," in *Proc. 6th Eur. Conf. Antennas Propag. (EUCAP)*, Mar. 2012, pp. 1276–1280.

[62] C. A. Balanis, *Advanced Engineering Electromagnetics* (CourseSmart Series). Hoboken, NJ, USA: Wiley, 2012.

[63] L. Bertel, J. Rojas-Varela, P. Gourvez, and D. Cole, "Polarisation and ground effects on HF receiving antenna patterns," *Ann. Télécommun.*, vol. 44, nos. 7–8, pp. 413–427, Jul. 1989.

[64] S. J. Orfanidis, *Electromagnetic Waves and Antennas*. Piscataway, NJ, USA: Rutgers Univ., 2011.

[65] S. R. Saunders and A. Aragón-Zavala, *Antennas and Propagation for Wireless Communication Systems*, 1st ed. New York, NY, USA: Wiley, 1999.

[66] P. Prats, A. Reigber, J. J. Mallorqui, R. Scheiber, and A. Moreira, "Estimation of the temporal evolution of the deformation using airborne differential SAR interferometry," *IEEE Trans. Geosci. Remote Sens.*, vol. 46, no. 4, pp. 1065–1078, Apr. 2008.

[67] B. Iglewicz and D. C. Hoaglin, *How to Detect and Handle Outliers* (ASQC Basic References in Quality Control). Tucson, AZ, USA: ASQC Quality Press, 1993.

[68] P. C. Hansen, "REGULARIZATION TOOLS: A MATLAB package for analysis and solution of discrete ill-posed problems," *Numer. Algorithms*, vol. 6, no. 1, pp. 1–35, Mar. 1994.

[69] P. C. Hansen, "Truncated singular value decomposition solutions to discrete ill-posed problems with ill-determined numerical rank," *SIAM J. Sci. Statist. Comput.*, vol. 11, no. 3, pp. 503–518, 1990. [Online]. Available: http://dx.doi.org/10.1137/0911028

[70] E. Trouvé, M. Caramma, and H. Maître, "Fringe detection in noisy complex interferograms," *Appl. Opt.*, vol. 35, no. 20, pp. 3799–3806, Jul. 1996.

[71] G. W. Davidson and R. Bamler, "Multiresolution phase unwrapping for SAR interferometry," *IEEE Trans. Geosci. Remote Sens.*, vol. 37, no. 1, pp. 163–174, Jan. 1999.

[72] D. W. Marquardt, "An algorithm for least-squares estimation of nonlinear parameters," *J. Soc. Ind. Appl. Math.*, vol. 11, no. 2, pp. 431–441, 1963.

[73] M. Kass, A. Witkin, and D. Terzopoulos, "Snakes: Active contour models," *Int. J. Comput. Vis.*, vol. 1, no. 4, pp. 321–331, 1988.

[74] C. Xu and J. L. Prince, "Gradient vector flow: A new external force for snakes," in *Proc. IEEE Conf. Comput. Vis. Pattern Recognit. (CVPR)*, Jun. 1997, pp. 66–71.

[75] C. Samson, L. Blanc-Féraud, J. Zerubia, and G. Aubert, "A level set model for image classification," in *Scale-Space Theories in Computer Vision* (Lecture Notes in Computer Science), M. Nielsen, P. Johansen, O. F. Olsen, and J. Weickert, Eds. Berlin, Germany: Springer, 1999, pp. 306–317.

[76] T. F. Chan and L. A. Vese, "Active contours without edges," *IEEE Trans. Image Process.*, vol. 10, no. 2, pp. 266–277, Feb. 2001.

[77] L. A. Vese and T. F. Chan, "A multiphase level set framework for image segmentation using the Mumford and Shah model," *Int. J. Comput. Vis.*, vol. 50, no. 3, pp. 271–293, Dec. 2002.

[78] A. Dubrovina, G. Rosman, and R. Kimmel, "Active contours for multi-region image segmentation with a single level set function," in *Scale Space and Variational Methods in Computer Vision* (Lecture Notes in Computer Science), vol. 7893, A. Kuijper, K. Bredies, T. Pock, and H. Bischof, Eds. Berlin, Germany: Springer, 2013, pp. 416–427.

[79] M. S. Horritt, "A statistical active contour model for SAR image segmentation," *Image Vis. Comput.*, vol. 17, nos. 3–4, pp. 213–224, Mar. 1999.

[80] I. B. Ayed, A. Mitiche, and Z. Belhadj, "Multiregion level-set partitioning of synthetic aperture radar images," *IEEE Trans. Pattern Anal. Mach. Intell.*, vol. 27, no. 5, pp. 793–800, May 2005.

[81] I. B. Ayed, A. Mitiche, and Z. Belhadj, "Polarimetric image segmentation via maximum-likelihood approximation and efficient multiphase level-sets," *IEEE Trans. Pattern Anal. Mach. Intell.*, vol. 28, no. 9, pp. 1493–1500, Sep. 2006.

[82] M. Silveira and S. Heleno, "Separation between water and land in SAR images using region-based level sets," *IEEE Geosci. Remote Sens. Lett.*, vol. 6, no. 3, pp. 471–475, Jul. 2009.

[83] W. Feng, W. Gang, V. Prinet, and R. Kun, "Phase unwrapping based on active contour model," in *Proc. IEEE Int. Geosci. Remote Sens. Symp. (IGARSS)*, vol. 7. Jul. 2003, pp. 4386–4388.

[84] K. Sartor, J. Allen, E. Ganthier, B. Gilbert, and G. B. Tenali, "Method and apparatus for processing complex interferometric SAR data," CA Patent 2 681 742, Sep. 25, 2008.

[85] S. Osher and J. A. Sethian, "Fronts propagating with curvature-dependent speed: Algorithms based on Hamilton–Jacobi formulations," *J. Comput. Phys.*, vol. 79, no. 1, pp. 12–49, Nov. 1988.

[86] M. Lucido, F. Meglio, V. Pascazio, and G. Schirinzi, "Closed-form evaluation of the second-order statistical distribution of the interferometric phases in dual-baseline SAR systems," *IEEE Trans. Signal Process.*, vol. 58, no. 3, pp. 1698–1707, Mar. 2010.

[87] A. Hooper, P. Segall, and H. Zebker, "Persistent scatterer interferometric synthetic aperture radar for crustal deformation analysis, with application to Volcán Alcedo, Galápagos," *J. Geophys. Res., Solid Earth*, vol. 112, no. B7, Jul. 2007.

[88] D. L. Donoho and J. M. Johnstone, "Ideal spatial adaptation by wavelet shrinkage," *Biometrika*, vol. 81, no. 3, pp. 425–455, 1994.

[89] M. Kazubek, "Wavelet domain image denoising by thresholding and Wiener filtering," *IEEE Signal Process. Lett.*, vol. 10, no. 11, pp. 324–326, Nov. 2003.

[90] F. Luisier, T. Blu, and M. Unser, "A new SURE approach to image denoising: Interscale orthonormal wavelet thresholding," *IEEE Trans. Image Process.*, vol. 16, no. 3, pp. 593–606, Mar. 2007.

[91] G. Chen and S.-E. Qian, "Denoising of hyperspectral imagery using principal component analysis and wavelet shrinkage," *IEEE Trans. Geosci. Remote Sens.*, vol. 49, no. 3, pp. 973–980, Mar. 2011.

[92] Y. Ding and I. W. Selesnick, "Artifact-free wavelet denoising: Non-convex sparse regularization, convex optimization," *IEEE Signal Process. Lett.*, vol. 22, no. 9, pp. 1364–1368, Sep. 2015.
[93] F. Argenti and L. Alparone, "Speckle removal from SAR images in the undecimated wavelet domain," *IEEE Trans. Geosci. Remote Sens.*, vol. 40, no. 11, pp. 2363–2374, Nov. 2002.
[94] A. Achim, P. Tsakalides, and A. Bezerianos, "SAR image denoising via Bayesian wavelet shrinkage based on heavy-tailed modeling," *IEEE Trans. Geosci. Remote Sens.*, vol. 41, no. 8, pp. 1773–1784, Aug. 2003.
[95] M. I. H. Bhuiyan, M. O. Ahmad, and M. N. S. Swamy, "Spatially adaptive wavelet-based method using the cauchy prior for denoising the SAR images," *IEEE Trans. Circuits Syst. Video Technol.*, vol. 17, no. 4, pp. 500–507, Apr. 2007.
[96] C. Lopez-Martinez and X. Fabregas, "Modeling and reduction of SAR interferometric phase noise in the wavelet domain," *IEEE Trans. Geosci. Remote Sens.*, vol. 40, no. 12, pp. 2553–2566, Dec. 2002.
[97] X. Zha, R. Fu, Z. Dai, and B. Liu, "Noise reduction in interferograms using the wavelet packet transform and Wiener filtering," *IEEE Geosci. Remote Sens. Lett.*, vol. 5, no. 3, pp. 404–408, Jul. 2008.
[98] Y. Bian and B. Mercer, "Interferometric SAR phase filtering in the wavelet domain using simultaneous detection and estimation," *IEEE Trans. Geosci. Remote Sens.*, vol. 49, no. 4, pp. 1396–1416, Apr. 2011.
[99] A. Ferretti, C. Prati, and F. Rocca, "Multibaseline InSAR DEM reconstruction: The wavelet approach," *IEEE Trans. Geosci. Remote Sens.*, vol. 37, no. 2, pp. 705–715, Mar. 1999.
[100] M. Shirzaei and R. Bürgmann, "Topography correlated atmospheric delay correction in radar interferometry using wavelet transforms," *Geophys. Res. Lett.*, vol. 39, no. 1, p. L01305, 2012.
[101] S. G. Mallat, "A theory for multiresolution signal decomposition: The wavelet representation," *IEEE Trans. Pattern Anal. Mach. Intell.*, vol. 11, no. 7, pp. 674–693, Jul. 1989.
[102] J. Portilla, V. Strela, M. J. Wainwright, and E. P. Simoncelli, "Image denoising using scale mixtures of Gaussians in the wavelet domain," *IEEE Trans. Image Process.*, vol. 12, no. 11, pp. 1338–1351, Nov. 2003.
[103] B. Goossens, A. Pizurica, and W. Philips, "Wavelet domain image denoising for non-stationary noise and signal-dependent noise," in *Proc. IEEE Int. Conf. Image Process.*, Oct. 2006, pp. 1425–1428.
[104] W. Y. Lo and I. W. Selesnick, "Wavelet-domain soft-thresholding for non-stationary noise," in *Proc. Int. Conf. Image Process.*, Oct. 2006, pp. 1441–1444.
[105] I. Atkinson, F. Kamalabadi, S. Mohan, and D. L. Jones, "Asymptotically optimal blind estimation of multichannel images," *IEEE Trans. Image Process.*, vol. 15, no. 4, pp. 992–1007, Apr. 2006.
[106] S. Mallat, *A Wavelet Tour of Signal Processing: The Sparse Way*, 3rd ed. San Francisco, CA, USA: Academic, 2008.
[107] I. Daubechies, *Ten Lectures on Wavelets*. Philadelphia, PA, USA: SIAM, 1992.
[108] G. Ferraiuolo, F. Meglio, V. Pascazio, and G. Schirinzi, "DEM reconstruction accuracy in multichannel SAR interferometry," *IEEE Trans. Geosci. Remote Sens.*, vol. 47, no. 1, pp. 191–201, Jan. 2009.
[109] L. I. Rudin, S. Osher, and E. Fatemi, "Nonlinear total variation based noise removal algorithms," *Phys. D, Nonlinear Phenomena*, vol. 60, nos. 1–4, pp. 259–268, 1992.
[110] F. Bovenga, V. M. Giacovazzo, A. Refice, and N. Veneziani, "Multichromatic analysis of InSAR data," *IEEE Trans. Geosci. Remote Sens.*, vol. 51, no. 9, pp. 4790–4799, Sep. 2013.

Muriel Pinheiro was born in Ribeirão Preto, Brazil, in 1986. She received the B.S. degree in electronic engineering and the M.S. degree in telecommunications from the Aeronautical Technological Institute, São José dos Campos, Brazil, in 2009 and 2010, respectively, and the Dr. Eng. degree (Hons.) from the Karlsruhe Institute of Technology, Karlsruhe, Germany, in 2016.

From 2009 to 2010, she was with BRADAR, Sao Jose dos Campos, Brazil, where she was involved in the development of calibration algorithms for airborne SAR interferometry (InSAR). In 2011, she joined the Microwaves and Radar Institute, German Aerospace Center, Wessling, Germany, where she has been a member of the Multimodal Algorithms Group. Her research interests include signal and image processing, advanced techniques for SAR image formation, InSAR, high-resolution digital elevation model generation, and persistent scatterer interferometry.

Andreas Reigber (M'02–SM'10–F'16) received the Diploma degree in physics from the University of Konstanz, Konstanz, Germany, in 1997, the Ph.D. degree from the University of Stuttgart, Stuttgart, Germany, in 2001, and the Habilitation degree from the Berlin University of Technology, Berlin, Germany, in 2008.

He is currently the Head of the SAR Technology Department, Microwave and Radar Institute, German Aerospace Center, Wessling, Germany, where he is leading the development and operation of state-of-the-art airborne SAR sensors. He is also a Professor of remote sensing and digital image processing with the Technische Universität Berlin, Berlin. His research interests include various aspects of multimodal, multichannel, and high-resolution SAR processing and postprocessing.

Dr. Reigber has received several prize paper awards, among them the IEEE TGRS Transactions Prize Paper Award in 2001 and 2016 for his works on polarimetric SAR tomography and nonlocal speckle filtering, respectively, and also the IEEE TGRS Letters Prize Paper Award in 2006 for his work on multipass SAR processing.

Rolf Scheiber received the Diploma degree in electrical engineering from the Technical University of Munich, Munich, Germany, in 1994, and the Ph.D. degree in electrical engineering from the University of Karlsruhe, Karlsruhe, Germany, in 2003. His Ph.D. thesis was on airborne SAR interferometry (InSAR).

Since 1994, he has been with the Microwaves and Radar Institute, German Aerospace Center, Wessling, Germany, where he has developed the first operational high-precision interferometric SAR processor for its E-SAR airborne sensor. Since 2001, he has been the Head of the SAR Signal Processing Group, SAR Technology Department, where he is currently supervising the F-SAR and Digital Beamforming Synthetic Aperture Radar airborne SAR processing activities. He also supported several ESA projects, including the Sentinel Program with several activities related to the demonstration with TerraSAR-X of the new Terrain Observation by Progressive Scan imaging mode. His research interests include algorithm development for airborne and spaceborne SAR focusing, InSAR, differential InSAR, SAR tomography, circular SAR, and also radio ice-sounding algorithms and applications.

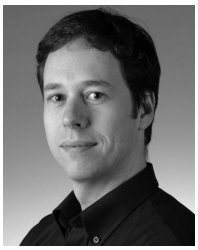

Pau Prats-Iraola (S'03–M'06–SM'13) was born in Madrid, Spain, in 1977. He received the Ingeniero and Ph.D. degrees in telecommunications engineering from the Universitat Politècnica de Catalunya (UPC), Barcelona, Spain, in 2001 and 2006, respectively.

In 2001, he was a Research Assistant with the Institute of Geomatics, Castelldefels, Spain. In 2002, he was with the Department of Signal Theory and Communications, UPC, where he was involved in the field of airborne repeat-pass interferometry and airborne differential SAR interferometry (InSAR). From 2002 to 2006, he was an Assistant Professor with the Department of Telecommunications and Systems Engineering, Universitat Autònoma de Barcelona, Barcelona. In 2006, he joined the Microwaves and Radar Institute, German Aerospace Center, Wessling, Germany, where he has been the Head of the Multimodal Algorithms Group since 2009. He has co-authored about 50 peer-reviewed journal papers in the field. His research interests include high-resolution airborne/spaceborne monostatic/bistatic SAR processing, InSAR, advanced interferometric acquisition modes, persistent scatterer interferometry, SAR tomography, and end-to-end SAR simulation.

Alberto Moreira (M'92–S'96–F'04) received the B.S.E.E. and M.S.E.E. degrees from the Aeronautical Technological Institute, São José dos Campos, Brazil, in 1984 and 1986, respectively, and the Dr. Eng. degree (Hons.) from the Technical University of Munich, Munich, Germany, in 1993.

From 1996 to 2001, he was a Chief Scientist and an Engineer with the SAR Technology Department, German Aerospace Center (DLR), Wessling, Germany. Under his leadership, the DLR airborne SAR system has been upgraded to operate in innovative imaging modes, such as polarimetric SAR interferometry and SAR tomography. Since 2001, he has been the Director of the Microwaves and Radar Institute, DLR, and a Full Professor with the Karlsruhe Institute of Technology, Karlsruhe, Germany, in the field of microwave remote sensing. His DLR's Institute contributes to several scientific programs and projects for spaceborne SAR missions, such as TerraSAR-X, TanDEM-X, SAR-Lupe, and SAR-Lupe follow-on and also Kompsat-6, PAZ, Sentinel-1, BIOMASS, and Tandem-L. The mission TanDEM-X, led by his Institute, has generated a global, high-resolution digital elevation model of the Earth with unprecedented accuracy, in which he served as an Initiator and a Principal Investigator. He has authored or co-authored over 350 publications in international conferences and journals and eight book chapters. He holds 21 patents in the radar and antenna field. His research interests include encompass spaceborne radar end-to-end system design, microwave techniques and system concepts, signal processing, and remote sensing applications.

Dr. Moreira has served as the President of the IEEE Geoscience and Remote Sensing Society (GRSS) in 2010. He was a recipient of several international awards, including the IEEE AESS Nathanson Award in 1999 for the Young Radar Engineer of the Year, the IEEE Kiyo Tomiyasu Field Award in 2007, the IEEE W.R.G. Baker Award from the IEEE Board of Directors in 2012, and the IEEE GRSS Distinguished Achievement Award in 2014. He and his colleagues received the GRSS Transactions Prize Paper Award in 1997, 2001, and 2007, respectively, and the GRSS Letters Prize Paper Award in 2015 and 2017, respectively. He was the Founder and the Chair of the GRSS German Chapter from 2003 to 2008. He served as an Associate Editor for the IEEE GEOSCIENCE AND REMOTE SENSING LETTERS from 2003 to 2007. He has been serving as an Associate Editor for the IEEE TRANSACTIONS ON GEOSCIENCE AND REMOTE SENSING since 2005. Since 2012, he has been serving as the Principal Investigator for the Helmholtz Alliance—Remote Sensing and Earth System Dynamics, comprising of 18 research institutes and 30 associated international partners.